Development of the Trigger Algorithm for the MONOLITH Experiment

Diplomarbeit am II. Institut für Experimentalphysik der Universität Hamburg

Oliver Gutsche
Hohenbergen 38
D-24558 Henstedt-Ulzburg

Hamburg, im April 2001

Abstract

The MONOLITH project is proposed to prove atmospheric neutrino oscillations and to improve the corresponding measurements of Super-Kamiokande. The MONOLITH detector consists of a massive (34 kt) magnetized iron tracking calorimeter and is optimized for muon neutrino detection. This diploma thesis presents the development of the trigger algorithm for the MONOLITH experiment and related test measurements.

Chapter two gives an introduction to the mechanism of neutrino oscillations. The two flavor approximation and the three flavor mechanism are described and influences of matter on neutrino oscillations are discussed. The principles of neutrino oscillation experiments are discussed and the results of Super-Kamiokande, a neutrino oscillation experiment, are presented. Super-Kamiokande gave the strongest indications for atmospheric neutrino oscillations so far.

The third chapter introduces the MONOLITH project in the context of atmospheric neutrino oscillations. The MONOLITH detector is described and the main active component, the glass spark chamber, is presented.

Chapter four presents the practical part of this thesis. A test setup of a glass spark chamber is built up including a cosmics trigger and a data acquisition system. Cosmic ray muons are used for the investigation of the chamber. During a long term test, the stability of the efficiency and the noise rate of the chamber are investigated. A status report of the results is given. The results are taken as input for the trigger development.

In chapter five, the development of the trigger algorithm is presented. In the beginning, the structural design of the trigger algorithm is described. The efficiency and the rate of the trigger algorithm are investigated using two event sources, a Monte Carlo neutrino event sample and a generated noise sample. For the analysis, the data sources are processed by several processing stages which are visualized by corresponding event displays. In the course of the data processing, dead zones of the detector are implemented. The optimization of several trigger parameter combinations results in the standard trigger algorithm. This algorithm is investigated in detail and the influences of possible changes in detector parameters are analyzed. In the end, the performance of the standard trigger algorithm is presented. The agreement with the requirements is confirmed.

Zusammenfassung

Um Oszillationen von atmosphärischen Neutrinos nachzuweisen und die diesbezüglichen Messungen von Super-Kamiokande zu verbessern, wurde das MONOLITH-Projekt zur Genehmigung vorgeschlagen. MONOLITH besteht aus einem 34 kt schweren magnetisierten Eisen-Spur-Kalorimeter und ist für den Nachweis von Myon-Neutrinos optimiert. In dieser Diplomarbeit werden die Entwicklung des Triggers für den MONOLITH-Detektor und damit verbundene Test-Messungen präsentiert.

In Kapitel zwei wird die Theorie der Neutrino-Oszillationen eingeführt und die Zwei-Familien-Näherung und der Drei-Familien-Fall näher beschrieben. Zusätzlich wird auf den Einfluss von Materie auf die Oszillationen eingegangen.

Die Grundzüge von Neutrino-Oszillations-Experimenten werden erläutert und das Super-Kamiokande-Experiment kurz beschrieben. Super-Kamiokande hat die bisher stärksten Hinweise auf Oszillationen der atmosphärischen Neutrinos gegeben.

Das dritte Kapitel beschreibt das MONOLITH-Projekt mit Bezug auf Neutrino-Oszillationen. Desweiteren wird eine Beschreibung des Detektors gegeben und die Haupt-Nachweis-Komponente, die Glas-Funken-Kammer, näher erläutert.

Das vierte Kapitel beschreibt den praktischen Teil der Diplomarbeit. Ziel des Laborpraktikums ist der Aufbau eines Teststandes einer einzelnen Glas-Funken-Kammer und die Durchführung eines Langzeittests. Mit Hilfe von kosmischen Myonen wird die Langzeit-Stabilität von Effizienz und Rausch-Rate der Kammer untersucht. Als Zusammenfassung wird ein Status-Bericht des Langzeittests gegeben, dessen Ergebnisse direkt in die Trigger-Entwicklung mit einfließen.

Die Entwicklung des Trigger-Algorithmus für den MONOLITH-Detektor wird in Kapital fünf beschrieben. Der strukturelle Aufbau des Algorithmus wird eingeführt und die zwei Ereignis-Quellen, die zur Untersuchung von Effizienz und Trigger-Rate des Algorithmus benutzt werden, werden beschrieben. Zur Analyse werden die Datenquellen in mehreren Schritten verarbeitet, unter anderem durch die Einführung von Totzonen des Detektors. Die Schritte inklusive mehrerer Event-Displays werden erläutert.

Am Ende wird die Optimierung des Trigger-Algorithmus beschrieben und der daraus gewonnene Standard-Trigger-Algorithmus näher untersucht. Desweiteren wird der Einfluss von Änderungen der Detektor-Parameter auf die Trigger-Rate untersucht. Am Ende wird die Übereinstimmung der Trigger-Effizienz und der Trigger-Rate mit den Vorgaben aufgezeigt.

Contents

1 Introduction **1**

2 Neutrino Oscillations **3**
2.1 Neutrinos in the Standard Model 3
2.1.1 Interactions of Neutrinos 5
2.2 Neutrino Oscillation Mechanism 6
2.2.1 Two Flavor Approximation 9
2.2.2 Three Flavor Neutrino Oscillations 10
2.2.3 Matter Effects 11
2.3 Observation of Neutrino Oscillations 12
2.3.1 Detection Methods 12
2.3.2 Neutrino sources 14
2.4 Super-Kamiokande 17

3 The MONOLITH Experiment **19**
3.1 Introduction to the MONOLITH Project 20
3.1.1 Goals 21
3.1.2 Oscillation Pattern 21
3.1.3 Principle of neutrino detection 24
3.2 The MONOLITH Detector 25
3.2.1 Detector Design 25
3.2.2 Main Active Component 26
3.2.3 Detector Construction 29

4 Test Setup **33**
4.1 Goals 33
4.2 Cosmics Trigger 34
4.3 Single GSC Setup 36
4.4 Data Acquisition 38
4.5 Status Report of the Long Term Test 41

5 Trigger Development **45**
5.1 Basics of a Trigger 45
5.2 Components of the Trigger Rate 47
5.2.1 Neutrino Events 47
5.2.2 Cosmic Muon Background 47
5.2.3 GSC Single Hit Rate 48
5.3 Design of the Trigger Algorithm 48
5.4 Data sources 51
5.4.1 Monte Carlo Generated Events 52
5.4.2 Noise Simulation 54
5.5 Data Processing 56
5.5.1 Read Procedure 57
5.5.2 Oscillation Analysis Cuts 57
5.5.3 Dead Zones 58
5.5.4 Trigger Procedure 62
5.5.5 Event Displays 63
5.6 Trigger Investigation 66
5.6.1 Trigger Optimization 66
5.6.2 Dependence on Detector Design 72
5.6.3 Result 75

6 Summary and Conclusion **77**

A Cosmics Trigger **79**
A.1 Scintillator Signal 81
A.2 Signal Chain 82
A.3 Gate Chain 82
A.4 Calibration 83

B Fluxmeter Calibration **85**

Bibliography **87**

Chapter 1

Introduction

In the standard model [1], neutrinos are massless. Nowadays, indications of neutrinos with mass get steadily more striking [2, 3]. One of the main approaches to determine the neutrino mass is based on the principle of neutrino oscillations [4], which proves that neutrinos have mass via the violation of the lepton flavor number conservation. Experiments which exploit this principle can be classified via the corresponding source of neutrinos. The sun [5], the atmosphere [6] of the earth and reactor facilities [7] are often used as neutrino sources.

The most striking indications yet for neutrino oscillations were given by the Super-Kamiokande collaboration [8] in Japan via the investigation of the atmospheric neutrino flux. Although these results give significant evidence for neutrino oscillations, a direct proof or distinction from other explanations of the flux deviations can not be given, due to the limited detector resolution of the Super-Kamiokande detector.

Therefore, a new approach to investigate atmospheric neutrino oscillations is proposed by the MONOLITH collaboration (**M**assive **O**bservatory for **N**eutrino **O**scillations or **LI**mits on **TH**eir existence) [9]. The proposed MONOLITH detector consists of a massive (34 kt) magnetized tracking calorimeter and is optimized for detecting atmospheric muon neutrinos.

A direct measurement of the pattern of atmospheric neutrino oscillations can be performed with a sufficient resolution to distinguish the explanation of the flux deviations via the neutrino oscillations mechanism from other explanations.

This diploma thesis presents the development of the trigger algorithm for the MONOLITH detector and related test measurements.

After an introduction to the theory of neutrino oscillations, the features

of atmospheric neutrino experiments are discussed (see chapter 2).

The MONOLITH project is introduced and the MONOLITH detector is described (see chapter 3).

In the course of studies concerning the main detector component of MONOLITH, a test setup is built up consisting of a single active element. The test setup represents the practical part of this diploma thesis and its main goal is a long term test of this active element. A status report on the results of the long term test is given (see chapter 4).

These results are directly included in the following development of the trigger for the MONOLITH experiment. After an introduction to the event sources used for the analysis, the investigated trigger algorithm structure is described. Also the different processing steps including the implementation of the dead zone structure of the MONOLITH detector are presented. The analysis of different trigger algorithms is discussed which results in an optimized trigger algorithm. This algorithm is analyzed in detail (see chapter 5).

The resulting trigger algorithm is proposed to be realized in MONOLITH.

Chapter 2

Neutrino Oscillations

In the following, an answer to the questions what is known about neutrinos and how neutrino oscillations can change this picture is presented. First, neutrinos are described in the context of the standard model, a consistent description of particles and their interactions from small to large scales. In addition, neutrino interactions vital for neutrino experiments are shortly discussed. After an introduction of the mechanism of neutrino oscillations, the principles of neutrino oscillation experiments are presented. In the end, the Super-Kamiokande experiment which gave the first evidence for atmospheric neutrino oscillations is described. The results of Super-Kamiokande concerning neutrino oscillations are briefly discussed. They represent the basic motivation of the MONOLITH experiment, which is planned to improve the Super-Kamiokande results and to prove their interpretation as neutrino oscillation.

2.1 Neutrinos in the Standard Model

The universe including our world consists of a large variety of forms of matter. This complexity covers scales of several orders of magnitude. Nowadays, experiments are able to investigate the nature from scales of the order of 10^{-18} m to 10^{26} m. The standard model simplifies this picture by describing all forms of matter by means of a small number of constituents and a set of basic forces acting between them. The forces are described by force fields which are represented by exchange particles. Mathematically, the interaction of the force fields with the constituents and with themselves is described by gauge field theories [1]. In the following, a short description is given only of the parts of the standard model which are related to neutrinos.

Neutrinos belong to the basic constituents, which are composed of

leptons and quarks. All basic constituents have spin $\frac{1}{2}$. Leptons are found as free particles whereas quarks only appear in groups which form particles. These particles are called hadrons.

The leptons are the electron, the muon and the tauon and their neutral partners, the electron neutrino, the muon neutrino and the tauon neutrino. They are arranged in three families according to the lepton family or lepton flavor (L_i).

$$\begin{array}{ccccc} \begin{pmatrix} \nu_e \\ e^- \end{pmatrix} & \begin{pmatrix} \nu_\mu \\ \mu^- \end{pmatrix} & \begin{pmatrix} \nu_\tau \\ \tau^- \end{pmatrix} & \begin{array}{l} Q = 0 \\ Q = -1 \end{array} & (2.1) \\ L_e = 1 & L_\mu = 1 & L_\tau = 1 & & \\ \begin{pmatrix} \bar{\nu}_e \\ e^+ \end{pmatrix} & \begin{pmatrix} \bar{\nu}_\mu \\ \mu^+ \end{pmatrix} & \begin{pmatrix} \bar{\nu}_\tau \\ \tau^+ \end{pmatrix} & \begin{array}{l} Q = 0 \\ Q = +1 \end{array} & (2.2) \\ L_e = -1 & L_\mu = -1 & L_\tau = -1 & & \end{array}$$

Neutrinos are considered by the standard model to be of zero mass and the number of standard model neutrinos is confirmed to be 3 according to experimental results [10].

In the standard model, the interactions between the basic constituents are described by 2 different forces: the strong and the electroweak force. The electroweak force developed from the unification of the electromagnetic and the weak force. The forces are described by force fields represented by exchange particles called exchange bosons.

Neutrinos only interact weakly. Therefore, only the weak force or interaction is needed to describe neutrino interactions. The exchange bosons of the weak interaction are the $W^\pm$ and the Z^0. The charge of the exchange boson results in two types of weak interactions.

Charged current interactions (CC) are described by the exchange of a $W^\pm$ boson. A neutrino which interacts by the exchange of a charged boson initiates a charged lepton of the same family in the final state due to the conservation of the lepton flavor number.

Neutral current (NC) interactions described by the exchange of a Z^0 boson are characterized by a neutrino in the initial and the final state.

Due to the high mass of the exchange bosons, at center-of-mass energies small compared to the mass of the exchange boson the cross section of neutrino interactions is small compared to electromagnetic and strong interactions between other basic constituents than neutrinos. The cross section is proportional to the neutrino energy E.

2.1.1 Interactions of Neutrinos

Experiments gain information about neutrinos by their detection. Since neutrinos only interact weakly, they do not leave tracks in a detector. Therefore all neutrino experiments depend on the detection of final state particles from neutrino interactions. The properties of the neutrinos are traced back from the final states of the interactions.

Detected CC neutrino interaction final states allow a direct reconstruction of the initial neutrino. Due to the flavor number conservation, the flavor of the initial neutrino is directly derived from the flavor of the final charged lepton (see figure 2.1).

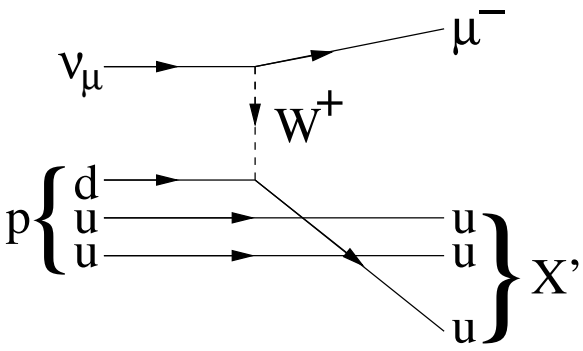

Figure 2.1: Feynman graph of an exemplary CC interaction between a neutrino and a proton. Shown are the initial neutrino (ν_μ) and initial hadron (p), the final charged lepton (μ^-) and the final hadronic components (X'). The CC interaction is described by the interaction between the neutrino and a quark of the hadron: $\nu_\mu d \rightarrow \mu^- u$.

For this thesis, only interactions between neutrinos and hadrons are relevant. In the following, only these neutrino interactions are considered. The interaction takes place between a quark of the initial hadron and the neutrino. The quark of the final state is not detected because a quark appears only combined with other quarks. Therefore, the hadronic final state consists of several hadrons resulting from the final quarks of the interaction.

Other possible interactions for neutrino detection are the NC interactions characterized by the exchange of a Z^0 boson (see figure 2.2). These interactions differ from CC interactions in the composition of the final state. In NC interactions, a neutrino is present in the initial and the final state. The final state neutrino escapes detection. Therefore, the flavor of the initial neutrino can not be reconstructed.

In the standard model, neutrino oscillations are not possible due to the

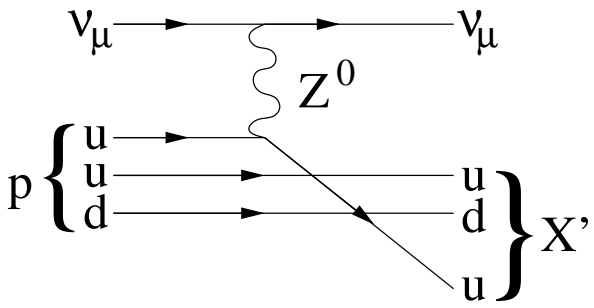

Figure 2.2: Feynman graph of an exemplary NC interaction between a neutrino and a proton. In contrast to the CC neutrino interaction (see figure 2.1), the initial and the final state contains a neutrino. The NC interaction is described by: $\nu_\mu u \rightarrow \nu_\mu u$.

conservation of the lepton flavor number and the zero mass of all three neutrinos. In the following, a description is given of a possibility of inclusion of neutrino oscillations into the standard model framework.

2.2 Neutrino Oscillation Mechanism

To add neutrino oscillations [11] to the existing formalism of the standard model, some requirements have to be fulfilled which go beyond the standard model assumptions:

- Not all neutrinos have equal mass, therefore not all neutrinos are massless.
- Lepton flavor numbers are not strictly conserved.

These requirements are not explicitly excluded by any basic principle. There are no underlying gauge principles which result in zero mass of all three neutrinos and in the conservation of lepton flavor numbers.

In quantum theory, the measurement of physical properties like the mass or the lepton flavor number are represented by operators. The operators are applied to the wave function or state which represents the investigated subject. The result of the measurement of the physical property is described by the resulting expression from the application of the operator. If the application of an operator on a state results in the same state multiplied with a factor, the state is called eigenstate and the factor eigenvalue. If the investigated state is an eigenstate to an operator, its corresponding eigenvalue

is an unambiguous characteristic of the investigated state. Otherwise, the investigated state is described by a superposition of different eigenstates.

The application of the α lepton flavor number operator $\mathcal{L}_\alpha$ on a neutrino eigenstate indicates if the eigenstate is a flavor α eigenstate or not.

$$\begin{aligned} \mathcal{L}_\alpha|\nu_\beta> &= \delta_{\alpha\beta}|\nu_\beta> \\ \mathcal{L}_\alpha|\bar{\nu}_\beta> &= -\delta_{\alpha\beta}|\bar{\nu}_\beta> \end{aligned}$$

In the case of zero mass of all neutrinos, the neutrino eigenstates to the three lepton flavor operators are also eigenstates to the mass operator $\mathcal{M}$.

Under the assumption of non-degenerate (i.e. non-zero) mass eigenstates $|\nu_i>$, the flavors are presented as superposition of the mass eigenstates and vice versa.

The general case, relevant for neutrino oscillations, consists of:

- flavor eigenstates $|\nu_\alpha>$: $<\nu_\alpha|\nu_\beta>=\delta_{\alpha\beta}$ related to the neutrino interactions
- mass eigenstates $|\nu_i>$: $<\nu_j|\nu_i>=\delta_{ij}$ related to the neutrino propagation

The mass and flavor eigenstates are connected via a unitary mixing matrix $\mathbf{U}$:

$$|\nu_\alpha> = \sum_i \mathbf{U}_{\alpha i}|\nu_i> \tag{2.3}$$

$$|\nu_i> = \sum_\alpha \left(\mathbf{U}^+\right)_{i\alpha}|\nu_\alpha> = \sum_\alpha \mathbf{U}^*_{\alpha i}|\nu_\alpha> \tag{2.4}$$

which includes n^2 parameters for an $n \times n$ matrix. These parameters are reduced to $(n-1)^2$ by fixing the $2n-1$ relative phases of the $2n$ neutrino states. Usually, the $\frac{1}{2}n(n-1)$ rotation angles of a n-dimensional rotation matrix (the weak mixing angles) and $\frac{1}{2}(n-1)(n-2)$ phases related to possible CP violation [12] are chosen.

In the following, the derivation of the transition probability for neutrino oscillations is described. The transition probability gives the probability for a neutrino of the flavor α and the energy E to change to a flavor β after a time t or, under the assumption that neutrinos travel at the speed of light, after traveling a distance $L = ct$.

To describe the probability, the time development for the eigenstates is needed:

$$|\nu_i(t)> = e^{-iE_it}|\nu_i(0)> \tag{2.5}$$

Assuming that neutrinos are stable and therefore E_i, the energy of the neutrino i, is real, the time development can be simplified with:

$$E_i = \sqrt{p^2 + m_i^2} \approx p + \frac{m_i^2}{2p} \approx E + \frac{m_i^2}{2E} \tag{2.6}$$

This simplification implies the assumption that all neutrinos i have equal momenta p and that the average neutrino energy for all neutrinos $E \approx p$ can be approximated by the momentum p. As a result, the energy differences between the neutrinos depend on their squared masses.

Starting from a pure $|\nu_\alpha>$ condition, the time development of the neutrino flavor $|\nu(0)>=|\nu_\alpha>$ is given by:

$$|\nu(t)>=\sum_i \mathbf{U}_{\alpha i} e^{-iE_i t}|\nu_i>=\sum_{i,\beta} \mathbf{U}_{\alpha i}\mathbf{U}^*_{\beta i} e^{-iE_i t}|\nu_\beta> \tag{2.7}$$

and results in the time dependent transition amplitude:

$$\begin{aligned} A(\alpha \to \beta, t) &= <\nu_\beta|\nu(t)> \\ &= \sum_i \mathbf{U}_{\alpha i}\mathbf{U}^*_{\beta i} e^{-iE_i t} \\ &= \sum_i \mathbf{U}_{\alpha i}\mathbf{U}^*_{\beta i} e^{-i\frac{m_i^2}{2}\frac{L}{E}} \end{aligned} \tag{2.8}$$

where a common phase factor is neglected and the distance between the $|\nu_\alpha>$-source and the detector $L = ct$ with $c = 1$ is included. This leads to the transition probability $P(\alpha \to \beta, t) = |A(\alpha \to \beta, t)|^2$:

$$\begin{aligned} P(\alpha \to \beta, t) &= \sum_{i,j} \mathbf{U}_{\alpha i}\mathbf{U}^*_{\alpha j}\mathbf{U}^*_{\beta i}\mathbf{U}_{\beta j} e^{i(E_i - E_j)t} \\ &= \underbrace{\sum_i |\mathbf{U}_{\alpha i}\mathbf{U}^*_{\beta i}|^2}_{\text{averaged transition probability}} + \underbrace{2\mathrm{RE}\sum_{j>i} \mathbf{U}_{\alpha i}\mathbf{U}^*_{\alpha j}\mathbf{U}^*_{\beta i}\mathbf{U}_{\beta j} e^{-i\frac{\delta m_{ij}^2}{2}\frac{L}{E}}}_{\text{time-dependent neutrino flavour oscillation}} \end{aligned} \tag{2.9}$$

where $\delta m_{ij}^2 = m_i^2 - m_j^2$. The measurement of the averaged transition probability only results in knowledge about transition matrix parameters, not about δm_{ij}^2.

Under the assumption of CP-invariance ($\mathbf{U}_{\alpha i}$ is real), the transition probability is given by:

$$P(\alpha \to \beta, t) = \delta_{\alpha\beta} - 4\sum_{j>i} \mathbf{U}_{\alpha i}\mathbf{U}_{\alpha j}\mathbf{U}_{\beta i}\mathbf{U}_{\beta j} sin^2\left(\frac{\delta m_{ij}^2}{4}\frac{L}{E}\right) \tag{2.10}$$

Expressed in common units, the exponential term can be written as:

$$sin^2\left(\frac{\delta m_{ij}^2}{4}\frac{L}{E}\right) = sin^2\left(1.267\frac{\delta m_{ij}^2}{\mathrm{eV}^2}\frac{L/km}{E/GeV}\right) \tag{2.11}$$

Starting from the general case of neutrino oscillations, several neutrino oscillations scenarios can be derived. Two possible scenarios, the two flavor approximation (see 2.2.1) and the three flavor neutrino oscillation (see 2.2.2) are described. In the end, dependencies of neutrino oscillations on the kind of medium penetrated by the neutrinos are briefly discussed.

2.2.1 Two Flavor Approximation

Simplifying the general case of a number of flavor and mass eigenstates, the two flavor approximation presents the simplest scenario of neutrino oscillations.

Starting with two flavor eigenstates ν_α, ν_β and two mass eigenstates ν_1, ν_2, the transition matrix **U** looks like:

$$\begin{pmatrix} \nu_\alpha \\ \nu_\beta \end{pmatrix} = \begin{pmatrix} cos(\theta) & sin(\theta) \\ -sin(\theta) & cos(\theta) \end{pmatrix} \begin{pmatrix} \nu_1 \\ \nu_2 \end{pmatrix} \tag{2.12}$$

with one transition matrix parameter $0 \leq \theta \leq \frac{\pi}{2}$. The maximal mixing case corresponds to $\theta = \frac{\pi}{4}$.

Derived from the general scenario, the transition probability is given by :

$$P(\nu_\alpha \to \nu_\alpha) = 1 - sin^2(2\theta)\, sin^2\left(\frac{\delta m^2}{4}\frac{L}{E}\right) \tag{2.13}$$

$$P(\nu_\alpha \to \nu_\beta) = sin^2(2\theta)\, sin^2\left(\frac{\delta m^2}{4}\frac{L}{E}\right) \tag{2.14}$$

The plot of the survival probability (2.13) indicates three regions depending on $\frac{L}{E}$ (see figure 2.3):

(a) $\frac{L}{E} \ll \frac{1}{\delta m^2}$**:** An oscillating effect is not visible due to a small oscillation frequency, i.e. the oscillations have not yet developed.

(b) $\frac{L}{E} \sim \frac{1}{\delta m^2}$**:** The oscillations can be resolved.

(c) $\frac{L}{E} \gg \frac{1}{\delta m^2}$**:** The oscillation frequency is too high to resolve the oscillation pattern with a limited detector resolution. Only the mixing between the two flavors ($sin^2(2\theta)$) can be observed.

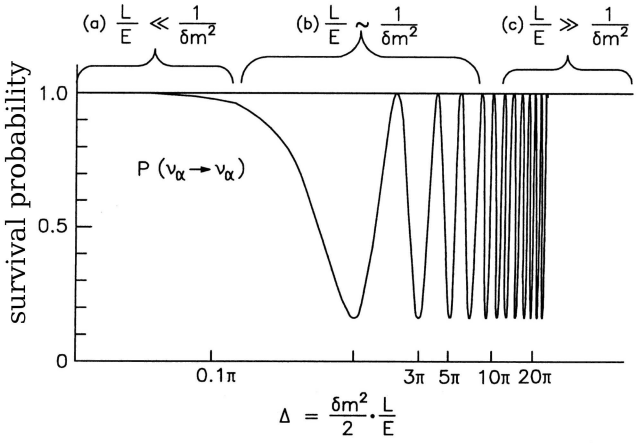

Figure 2.3: *Survival probability* versus $\Delta = \frac{\delta m^2}{2}\frac{L}{E}$ for $sin^2\ 2\theta = 0.83$ in logarithmic scale for Δ. Three regions: (a) oscillation can not yet be observed due to the small oscillation frequency for $\frac{L}{E} \ll \frac{1}{\delta m^2}$, (b) observation of oscillations for $\frac{L}{E} \sim \frac{1}{\delta m^2}$ is possible, (c) due to high oscillation frequency, the oscillation pattern can not be resolved for $\frac{L}{E} \gg \frac{1}{\delta m^2}$, only the mixing ($sin^2\,(2\theta)$) of the two flavors can be determined [13].

2.2.2 Three Flavor Neutrino Oscillations

The standard model quotes three different neutrino flavors. Starting from this point, the three neutrino flavor oscillation scenario (three flavor eigenstates ν_e, ν_μ, ν_τ and three mass eigenstates ν_1, ν_2, ν_3) requires three mixing angles $\theta_1, \theta_2, \theta_3$ ($0 \leq \theta_i \leq \frac{\pi}{2}$) and a CP-violating phase δ ($-\pi \leq \delta \leq \pi$) and results in two independent mass differences δm^2_{ij}. Similar to the *Cabibbo-Kobayashi-Maskawa-Matrix* [14], the transition matrix can be parametrisized by choosing the three Euler angles of a rotation in a three-dimensional space:

$$\begin{aligned} U &= \begin{pmatrix} 1 & 0 & 0 \\ 0 & c_2 & s_2 \\ 0 & -s_2 & c_2 \end{pmatrix} \begin{pmatrix} c_1 & s_1 & 0 \\ -s_1 & c_1 & 0 \\ 0 & 0 & 1 \end{pmatrix} \begin{pmatrix} 1 & 0 & 0 \\ 0 & 1 & 0 \\ 0 & 0 & e^{i\delta} \end{pmatrix} \begin{pmatrix} 1 & 0 & 0 \\ 0 & c_3 & s_3 \\ 0 & -s_3 & c_3 \end{pmatrix} \\ &= \begin{pmatrix} c_1 & s_1 c_3 & s_1 s_3 \\ -s_1 c_2 & c_1 c_2 c_3 - s_2 s_3 e^{-i\delta} & c_1 c_2 s_3 + s_2 c_3 e^{-i\delta} \\ s_1 s_2 & -c_1 s_2 c_3 - c_2 s_3 e^{-i\delta} & -c_1 s_2 s_3 + c_2 c_3 e^{-i\delta} \end{pmatrix} \end{aligned} \tag{2.15}$$

with $s_i = sin\theta_i$ and $c_i = cos\theta_i$.

The further treatment of the three neutrino flavor oscillations scenario results in complicated transition and survival probabilities [4] which are not necessary for the following descriptions.

2.2.3 Matter Effects

The neutrino oscillations mechanism presented so far only refers to the vacuum oscillations without any influence of matter.

While traveling through matter [15], the neutrino flavors interact differently with matter. The amplitude of the coherent forward scattering on nuclei and electrons is different for the neutrino flavors. This behavior is phenomenologically expressed in terms of a refractive index n in analogy to standard optics.

The forward scattering for ν_e and ν_μ is possible via NC interactions and induces a small non-zero value for $\epsilon = n - 1$, where ϵ has opposite sign for neutrino and anti-neutrino. In comparison to ν_μ, the ν_e has a somewhat larger forward scattering amplitude because of the possible CC interactions with the electrons of matter $\nu_e e^- \to \nu_e e^-$.

Considering neutrino oscillations in matter, all momenta p have to be substituted by np in the general mechanism (see 2.2) which induces an additional phase factor in the neutrino wave function.

In the three neutrino flavor framework with the ν_μ as a reference (only differences in this phase factor are relevant), the mass matrix includes additional terms and its diagonalization results in different mass eigenvalues compared to the vacuum scenario. The oscillation pattern (see figure 2.3) is disturbed by this effect and can show a different shape.

While passing through matter [16], it is possible that the oscillation reaches a maximum due to the changed mass eigenvalues and mixing angles, even though the vacuum oscillation is not maximal. This effect, called *Mikheyev-Smirnov-Wolfenstein*-effect (MSW-effect), can result in an effective change from ν_e to ν_μ and vice versa. It depends, amongst other things, on the electron density of the penetrated matter.

The MSW-effect occurs only when neutrinos pass through matter with a non-uniform electron density distribution. The impact of this density can result in a rotation of the flavor basis with respect to the muon eigenstates which induces the effective change of neutrino flavor.

In general, $\nu_\mu \to \nu_\tau$ oscillations do not show matter effects because both neutrino flavors have the same NC interactions with matter. Also matter effects are different for neutrinos and their anti-particles because of the opposite sign of their scattering amplitudes.

2.3 Observation of Neutrino Oscillations

2.3.1 Detection Methods

The detection of neutrino oscillations is based on two principles. The appearance method investigates in principle a flux of neutrinos of defined flavor and detects the appearance of a different flavor in this flux. The disappearance method compares measurements of a flux of neutrinos of defined flavor at several distances from the source and detects neutrino oscillations by a decreased flux of neutrinos beyond the trivial reduction depending on $\frac{1}{L^2}$ in the farer detectors with respect to the nearer detectors.

Appearance Method

The more direct method is based on the appearance of another flavor in a neutrino flux of defined flavor.

In the ideal case, a neutrino source produces a neutrino flux of a defined flavor ν_α. After a certain distance, a detector proves the appearance of a neutrino of the flavor ν_β with $\alpha \neq \beta$ via its CC interactions.

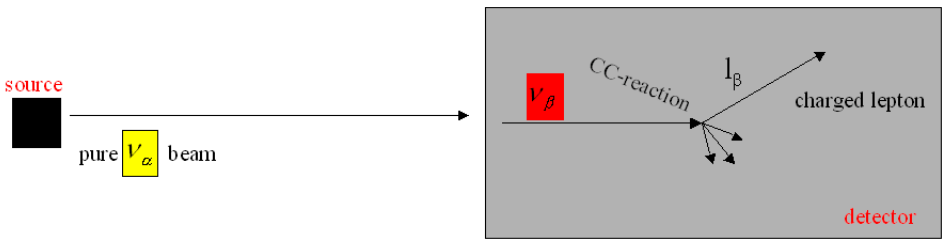

Figure 2.4: Appearance method: a neutrino source produces a neutrino flux of a defined flavor ν_α. After a certain distance, a detector proves the appearance of a neutrino of the flavor ν_β with $\alpha \neq \beta$ via its CC interactions and indicates a flavor changing effect.

This method implies several requirements:

1. The neutrino energy has to be large enough to produce the final state charged lepton for identification of the neutrino flavor (see 2.1.1).

2. The detector has to be able to distinguish the final state lepton from other final states.

Disappearance Method

This method is based on a very good control of the neutrino flux of flavor ν_α from the source or on a second detector **near** the source. This knowledge is compared with the measurements in the **far** detector where the same flavor ν_α is detected (see 2.1.1). The flavor changing effect is detected via a reduction of ν_α events in the far detector, if the neutrinos which changed flavor escape detection.

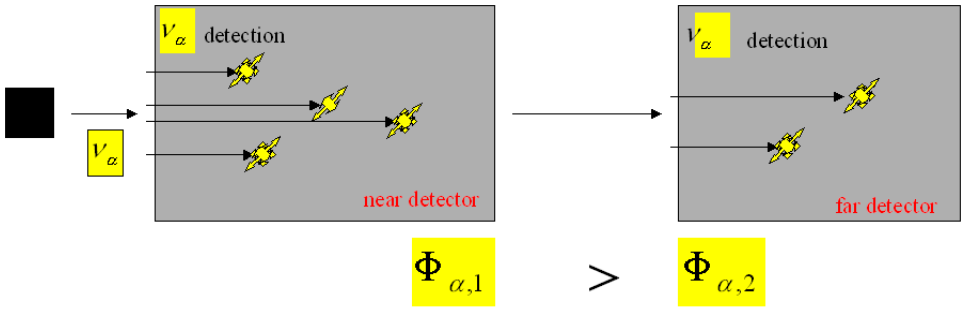

Figure 2.5: Disappearance method: a neutrino source produces a neutrino flux of a defined flavor ν_α. A **near** detector determines the flavor composition of the neutrino flux by detecting the CC interaction final states of ν_α, or the composition is predicted by simulations or models. The determination of the ν_α composition is repeated in the **far** detector. Any deviation between the near and far results indicates the flavor changing effect, if other flavors which appear after the near detector escape the detection in the far detector.

The requirements for the disappearance method are similar to the requirements of the appearance method:

1. The neutrino energy has again to be large enough for final state charged lepton production to ensure the identification of the neutrino flavor. The difference to the appearance method is connected to the possible oscillation partners. The appearance method requires the detection of all involved flavors of the oscillation. Therefore, the energy has to be sufficiently high to produce even the final state charged lepton with the highest mass. The disappearance method only requires the detection of only one final state charged lepton of the possible involved neutrino flavors. This has a large impact on the detector design. A detection of final state charged leptons with higher masses than the mass of the final state required by the disappearance method is not necessary.

2. The expected neutrino flux has to be under good control at the far detector either via a second near detector or via good knowledge of the expected neutrino source flux.

Possible realizations include either the usage of two detectors, one far and one near or the usage of several sources at different distances to the detector with equal neutrino flux properties.

2.3.2 Neutrino sources

Different sources can be used to obtain fluxes of sufficient intensity for neutrino oscillation experiments. Apart from the sun and a reactor as neutrino sources, accelerators play an important role. In combination with a detector with sufficient capabilites , these experiments can exploit both the appearance and disappearance methods. The accelerator experiments with a long distance between the source and the detectors are called **long baseline experiments**. On the other hand, also the atmosphere provides a neutrino flux which can be used for experiments.

The production of atmospheric neutrinos is initiated by cosmic radiation impinging on the atmosphere and interacting with its constituents. These particles decay to leptons and neutrinos (see figure 2.6).

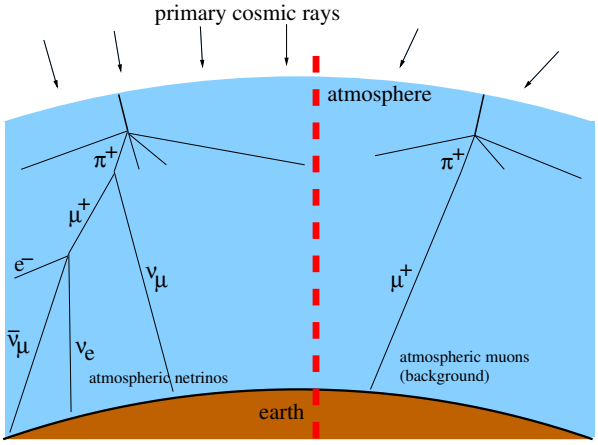

Figure 2.6: Production of atmospheric neutrinos. Primary cosmic rays (mainly protons) interact with particles of the atmosphere and produce shower particles which decay to leptons and neutrinos (*left side*). Not decaying muons represent the main background for atmospheric neutrino experiments (*right side*).

Mainly protons, but also heavier particles up to iron nuclei, produce atmospheric showers of pions and kaons which decay to leptons (see figure 2.7)

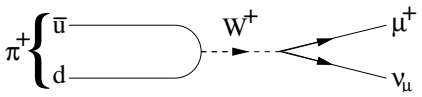

Figure 2.7: Feynman graph of an exemplary decay of shower particles resulting from cosmic radiation impinging the atmosphere. The displayed interaction is: $\pi^+ \rightarrow \mu^+ \nu_\mu$.

Furthermore, the leptons can further decay to lighter leptons and neutrinos (see figure 2.8).

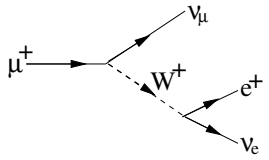

Figure 2.8: Further decaying lepton displayed by a exemplary Feynman graph. The displayed interaction is: $\mu^+ \rightarrow \bar{\nu}_\mu e^+ \nu_e$.

A typical atmospheric cascade (see figure 2.6 *left*) therefore produces a muon to electron neutrino ratio of:

$$\frac{\nu_\mu}{\nu_e} = \frac{2}{1} \tag{2.16}$$

The main background for atmospheric neutrino experiments consists of high energy $\mu^\pm$ which directly impinge on the surface.

For neutrino experiments there exist several advantages in using atmospheric neutrinos:

- Atmospheric neutrinos cover a very large range of $\frac{L}{E}$ (from $1\frac{km}{GeV}$ to $10^5\frac{km}{GeV}$). This enables the experiments to study a large range of oscillation parameters (see 2.2).
- For disappearance experiments, the scenario of a single detector with several sources at different distances can be realized (see 2.3.1). If the detector is built near the earth's surface, the neutrinos from directly above the detector (**downward**, $cos(\theta) > 0$) travel a distance

of $\sim 20\ km$, the neutrinos from the other side of the earth (**upward**, $cos(\theta) < 0$) the greater distance of $\leq 13.000\ km$ (see figure 2.9). There is a direct correlation between the traveled distance L and the zenith angle θ. The background from the not-decaying $\mu^{\pm}$ can be reduced by building the detector in an underground facility.

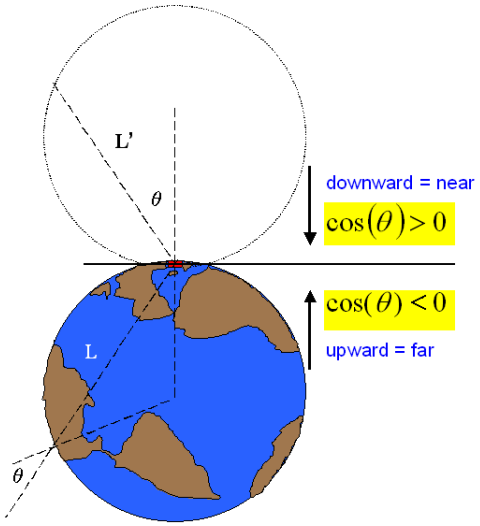

Figure 2.9: Sketch of underground disappearance experiment: the neutrinos from directly above the detector (**downward**, $cos(\theta) = 1$) travel a distance of $\sim 20\ km$, the neutrinos from the other side of the earth (**upward**, $cos(\theta) = -1$) the greater distance of $\sim 13.000\ km$.

One of the main advantages of the use of atmospheric neutrinos is the approximate equality of the primary upward neutrino flux with the primary downward neutrino flux, $N_\nu(cos(\theta)) \simeq N_\nu(-cos(\theta))$. This relation follows from simple geometrical arguments and results in the independence of the ratio of the two neutrino fluxes from the normalization.

- With the neutrino experiments existing nowadays, some special neutrino oscillations conditions can only be investigated with atmospheric neutrinos. For instance, the oscillation pattern (see figure 2.3) for low δm^2 [9] relative to the Super-Kamiokande central value (see 2.4) can only be detected with atmospheric neutrino experiments. Matter effects (see 2.2.3) also belong to the oscillation effects which can today only be investigated with atmospheric neutrinos [17].

2.4 Super-Kamiokande

The most striking evidence for atmospheric neutrino oscillations is given by the Super-Kamiokande collaboration [8].

The Super-Kamiokande detector (see figure 2.10) consists of a barrel filled with 50 kt clean water. The inner volume of 32 kt is surrounded by a layer of photomultiplier tubes, the outer cylinder walls are also covered with photomultipliers. The fiducial volume of Super-Kamiokande is about 25 kt.

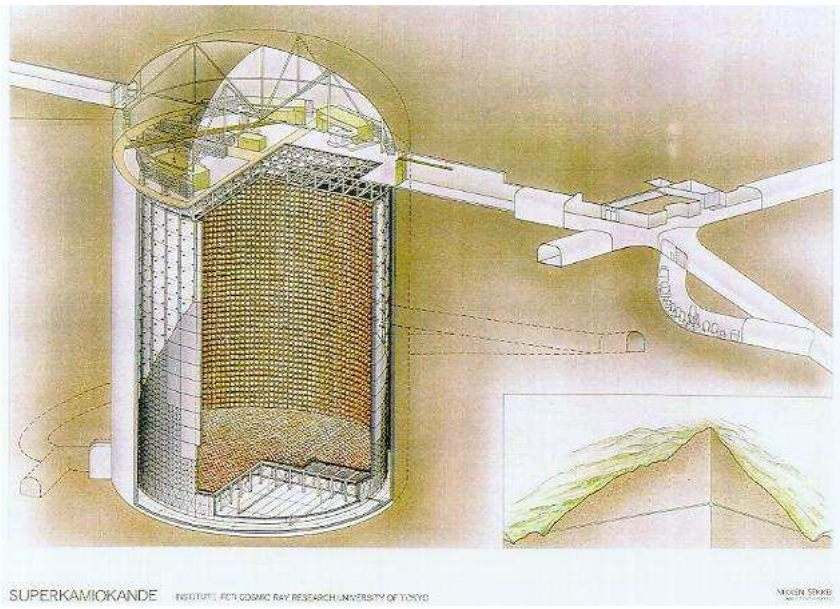

Figure 2.10: Super-Kamiokande detector sketch [18]

The charged particles, especially the charged leptons of neutrino interactions, are detected via their Čerenkov radiation and the different final state leptons ($e^{\pm}$ and $\mu^{\pm}$) are separated via their characteristic Čerenkov rings.

The results of the atmospheric neutrino event sample analysis (see fig 2.11) are divided into two energy ranges, the *sub-GeV* range for energies $\leq 1.33\ GeV$ and the *multi-GeV* range for energies $> 1.33\ GeV$. For each range, the number of events are displayed according to their flight direction ($cos(\theta)$) and separated into the two energy ranges and the produced final state leptons.

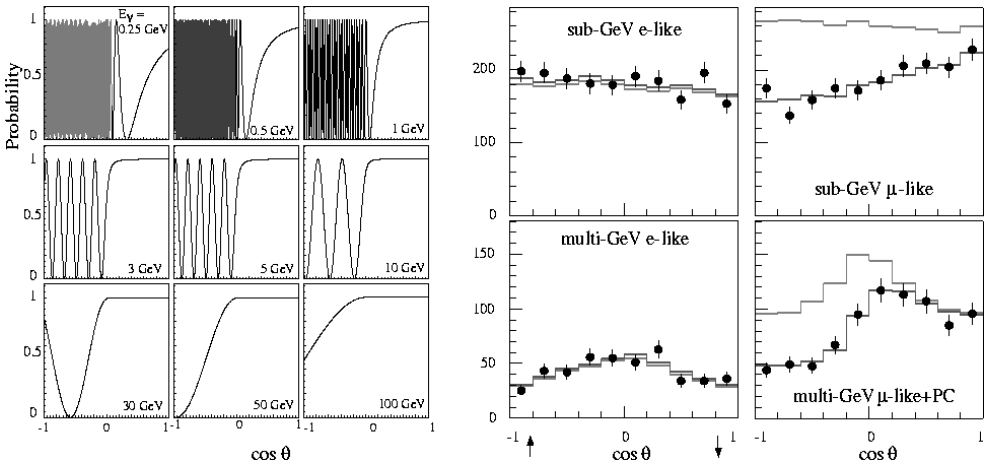

Figure 2.11: Super-Kamiokande results: *left side*: oscillation probability versus $cos(\theta)$ (oscillation effects only for upward going neutrinos ($cos(\theta) < 0$)) without detector resolution influence. *Right side*: measured event spectra versus $cos(\theta)$ separated according to e and μ events and compared to the non-oscillation hypothesis (grey line) and $\nu_\mu - \nu_\tau$ oscillation hypothesis (black line).

The electron plots do not show an effect, the data is compatible with the Monte Carlo simulations for the non-oscillation hypothesis. In the muon data, an effect is clearly visible. In the *sub-GeV* range, the non-oscillation hypothesis predicts more events over the complete $cos(\theta)$ range than measured with the Super-Kamiokande detector. Also this difference is larger for upward going neutrinos. On the other hand, the data is compatible with the oscillation hypothesis Monte Carlo simulation. The most striking effect is visible in the *multi-GeV* range. A deviation from the predicted flux is only visible for upward going neutrinos. For downward going muon neutrinos no effect is visible (the distance traveled for downward going neutrinos is too short for the oscillations to develop). The agreement with the oscillation hypothesis expectation results in the possible explanation of the suppressed rate of upward going ν_μ by maximal $\nu_\mu - \nu_\tau$ oscillations ($sin^2(2\theta) = 1$).

However, a direct proof of this oscillation hypothesis is not possible with the Super-Kamiokande detector. The resolution in $\frac{L}{E}$ is not sufficient to resolve the oscillation pattern. Also a distinction between other possible explanations of the measured effects, discussed in the following section, and the oscillation hypothesis is not realizable.

Chapter 3

The MONOLITH Experiment

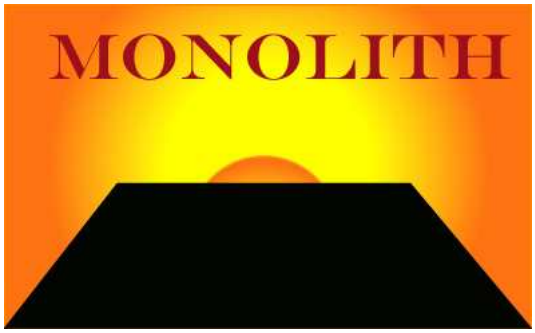

To confirm the indications for atmospheric neutrino oscillations given by the Super-Kamiokande collaboration (see 2.4), the MONOLITH experiment [9] is designed to prove or reject the hypothesis of atmospheric neutrino oscillations. The MONOLITH project is introduced (see 3.1) by the description of the project's goals (see 3.1.1). The main goal of MONOLITH, the observation of the atmospheric neutrino oscillation pattern (see 3.1.2) is presented in the context of the Super-Kamiokande results (see 2.4) and a short introduction to the principles of neutrino detection (see 3.1.3) with respect to MONOLITH is given.

In the second part, the MONOLITH detector (see 3.2) is presented. After a short presentation of the design of the detector, the main active component, the glass spark chamber, (see 3.2.2) is discussed. In the end, a description of the geometrical arrangement of the glass spark chambers within the MONOLITH detector is given which is important for the trigger development, the main topic of this thesis.

3.1 Introduction to the MONOLITH Project

The measurements of the Super-Kamiokande experiment concerning atmospheric neutrinos represent a strong hint for atmospheric neutrino oscillations (see 2.4). MONOLITH is designed to prove the oscillation hypothesis by direct observation of the oscillation pattern (see figure 2.3).

The observation requires the reconstruction of the $\frac{L}{E}$ ratio for each recorded neutrino event. Therefore, the MONOLITH detector consists of a massive magnetized tracking calorimeter, located in the underground laboratory in Gran Sasso, Italy, for investigation of the final states of neutrino CC interactions (see 2.1.1). MONOLITH is an underground disappearance experiment (see 2.3.1) and generally exploits the high energy component of atmospheric neutrinos (see 2.3.2). In the case that the atmospheric neutrino oscillations are confirmed, MONOLITH is designed to improve the measurement of the oscillation parameters with respect to former and current experiments.

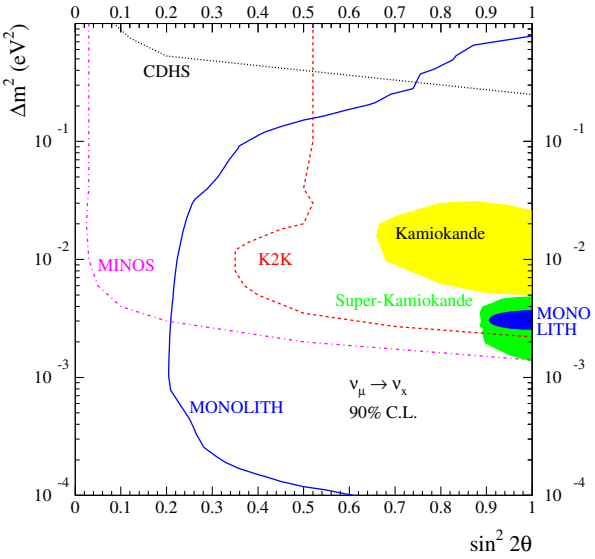

Figure 3.1: Sensitivity regions of oscillation parameters for ν_μ disappearance (see 2.2) in δm^2 versus $sin^2(2\theta)$. Listed are the expectations for K2K [19, 20] (5 years), MINOS [21] (3 years reference beam) and MONOLITH [9] (4 years). Also listed is the measured exclusion contour of CDHS [22] and allowed regions from Super-Kamiokande [23], Kamiokande [24] and a typical expected allowed region for MONOLITH (4 years for current Super-Kamiokande central value)

To classify MONOLITH in the context of actual and former neutrino oscillation experiments, the sensitivity and allowed regions of several experiments are displayed as a function of the oscillation parameters $sin^2(2\theta)$ and δm^2 (see figure 3.1). The region of oscillation parameters suggested by the Super-Kamiokande collaboration is fully covered. The expected allowed region of MONOLITH after 4 years data taking is smaller than the Super-Kamiokande allowed region due to the better resolution (see 3.1.2).

3.1.1 Goals

MONOLITH is optimized for detecting atmospheric muon neutrino events by their CC interactions (see 2.1.1). It is situated in the underground laboratory in Gran Sasso, Italy, and represents an underground disappearance experiment (see 2.3.1). The goals of the MONOLITH experiment cover several aspects of atmospheric neutrino oscillations.

1. The **main goal** is to prove or reject the hypothesis of atmospheric neutrino oscillations by the explicit observation of the first swing in the oscillation pattern (see figure 2.3) in ν_μ disappearance. Furthermore, MONOLITH investigates or excludes alternative explanations for observed neutrino flavor changing effects and achieves a significant improvement of the measurement of the oscillation parameters.

2. Further investigations of the atmospheric neutrino flux are made by charge and momentum measurements of the CC interaction final state muon in combination with the reconstruction of the energy of the hadronic system.

3. MONOLITH explores potential matter effects in atmospheric neutrino oscillations if the oscillation hypothesis is proved (see 2.2.3).

4. Cosmic ray muons up to the 100 TeV range are studied.

Referring to the main goal of MONOLITH, a short introduction to the oscillation pattern analysis is given.

3.1.2 Oscillation Pattern

The explicit observation of the oscillation pattern (see figure 2.3) is based on the comparison of ν_μ-CC events in the detector with predictions of atmospheric neutrino flux models and Monte Carlo simulations depending on the ratio of $\frac{L}{E}$ (see 2.2). A more sophisticated analysis based directly on

the up-down flux ratio [9] is not presented here. Therefore, a reconstruction of the $\frac{L}{E}$ ratio for each detected event is required and the resulting oscillation pattern depends on the accuracy of these measurements. The main improvement of the MONOLITH measurements with respect to the Super-Kamiokande results is the observation of the reappearance of the ν_μ flux at high $\frac{L}{E}$.

The Super-Kamiokande collaboration (see 2.4) performed a similar analysis and gained hints for atmospheric neutrino oscillations (see figure 2.11).

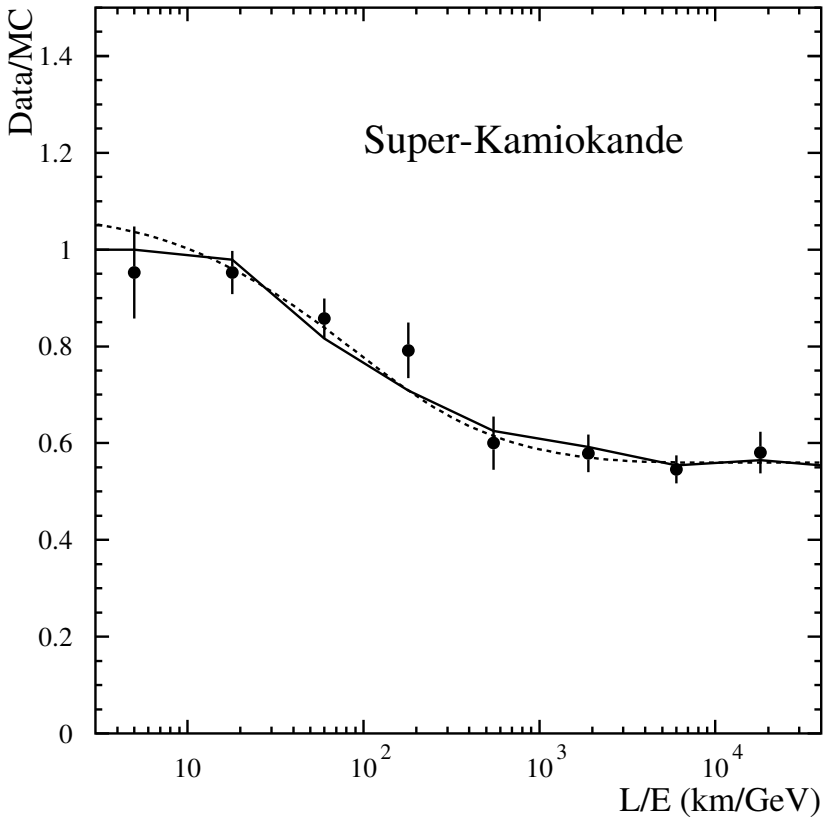

Figure 3.2: Oscillation pattern analysis by Super-Kamiokande collaboration [8]: measured (DATA) over predicted (MC) atmospheric neutrino events depending on $\frac{L}{E}$, smeared by detector resolution. A distinction of oscillation hypothesis (see 2.2)(black line) from a decay model [25] (dashed line) is not possible. A reappearance effect for large $\frac{L}{E}$ is not visible.

The distinction between the oscillations hypothesis (see 2.2) and other alternative explanations [25, 26, 27], especially a ν_μ decay model [25], cannot be done due to the insufficient resolution (see figure 3.2). The data points are compatible with both hypotheses.

MONOLITH is able to distinguish these hypotheses due to its better resolution. The observation of the reappearance at high $\frac{L}{E}$ is visible, if the atmospheric neutrino oscillations hypothesis is confirmed (see figure 3.3).

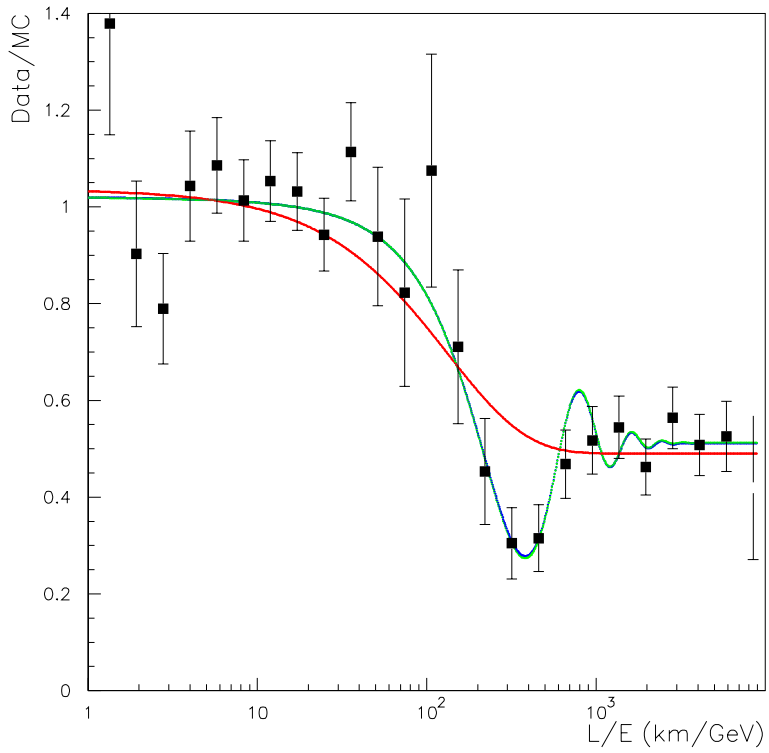

Figure 3.3: Oscillation pattern for MONOLITH: ratio of measured (DATA) over predicted (MC) atmospheric neutrino events. The data points are compared to the expected neutrino oscillation pattern including the MONOLITH detector resolution (light line) and to an expected neutrino decay model pattern also including the detector resolution (dark line). A reappearance of neutrinos can be directly observed.

In the following, the principles of neutrino detection with respect to atmospheric neutrinos and the MONOLITH project are shortly discussed.

3.1.3 Principle of neutrino detection

The measurement of the oscillation pattern implies the determination of the energy E and the flight direction or zenith angle θ for each neutrino event in the detector. To detect the oscillations pattern, the FWHM (full width at half maximum) error of the $\frac{L}{E}$ ratio has to be smaller than half of the modulation period (figure 2.3). This constrains the angular and energy resolution requirements of the detector. The flight direction of the neutrino is estimated by the muon flight direction. The higher the energy of the neutrino the smaller is the error of the estimation of the neutrino flight direction. A more accurate flight direction measurement improves the $\frac{L}{E}$ ratio resolution. This also has an impact on the event selection for the oscillation pattern analysis, because high energy events have a better resolution than low energy events.

The energy measurement of the neutrino is realized by the determination of the energy and the momenta of the CC interactions final states (figure 2.1).

The flight distance L is derived from the zenith angle θ (see figure 2.9).

$$L(\theta) \simeq R_{\text{earth}} \left(\sqrt{1 - k^2 sin^2(\theta)} - k|cos(\theta)| \right) \tag{3.1}$$

where $k = R_{\text{earth}}/(R_{\text{earth}} + \Delta R) \simeq 0.995$ and ΔR the average neutrino production height in the atmosphere [9].

The measurement of θ, the neutrino flight direction is done in the simplest experimental approach by the determination of the muon flight direction. If the vertex of the neutrino interaction is not identified, the direction determination gets more complex. In this case, one possibility to measure the sign of the flight direction is the time of flight method, which determines the direction by comparing the relative time informations of the hits along the muon track. This method requires a time resolution of the hits in the detector of the order of 1 ns.

For a measurement of the oscillation pattern a minimum number of neutrino interactions is required. Therefore, the detector need a large mass due to the small cross section of neutrino interactions and the limited atmospheric neutrino flux.

These requirements lead to the design of a massive tracking calorimeter [9], which is designed to consist of high-density material (iron) to reduce cost and space requirements.

In addition, a magnetic field which is a novelty in atmospheric neutrino experiments enhances the resolution and sensitivity range for the oscillation

parameters. The momentum measurement of the final state muons is obtained by range measurements in the detector. If the muon leaves the detector, a range measurement can not be performed. In this case, the momentum is measured by the curvature of the track.

3.2 The MONOLITH Detector

Here, a more detailed description of the MONOLITH detector presents the general detector design (see 3.2.1). After the description of the main active component (see 3.2.2), the construction of the detector out of these components is discussed (see 3.2.3).

3.2.1 Detector Design

The MONOLITH design consists of a large modular sandwich structure which is divided into two supermodules. Overall, it is composed of 121 horizontal 8 cm thick iron plates of 15 × 30 m^2 interleaved with gaps of 2 cm for the active detector elements. Its height is about 12 m and its total mass about 34 kt. The fiducial volume used for the oscillation pattern measurement corresponds to about 26 kt and is comparable with the Super-Kamiokande fiducial mass (see 2.4).

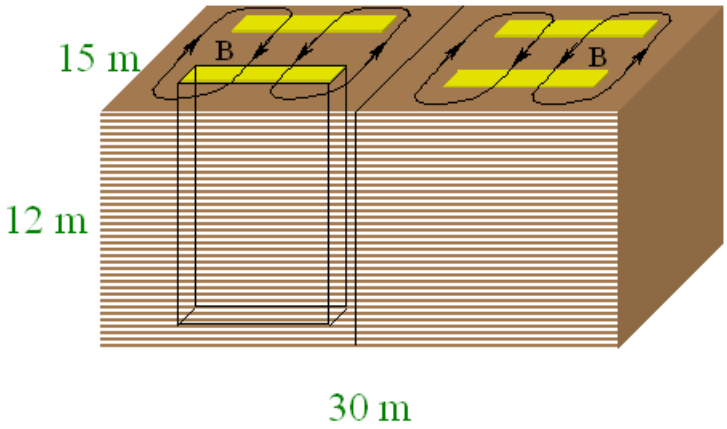

Figure 3.4: The MONOLITH detector is built out of 121 iron plates 15×30 m^2 wide and 8 cm thick interleaved with 2 cm thick gaps for active detector elements. A sketch of the coils and the resulting magnetic field lines is also shown.

The magnetic field in the iron has a strength of $1.2 - 1.4$ T. Each field line is confined to an individual iron plate to avoid huge power consumption and stray fields (see figure 3.4). Only the necessary vertical slots for the currents to generate the magnetic field disturb the horizontal homogeneity.

Furthermore, a scintillator layer as a veto surrounds the detector. The purpose of the veto is mainly to reduce the background from cosmic ray muons entering from the outside.

3.2.2 Main Active Component

The MONOLITH detector consists of 54.000 m^2 of active detector components. Therefore, a low cost detector manufactured in mass production is required. These requirements are fulfilled by the **Glass Spark Chamber** (GSC) [28, 29, 30, 31, 32, 33, 34, 35] (see figure 3.5), a *resistive plate chamber* (RPC).

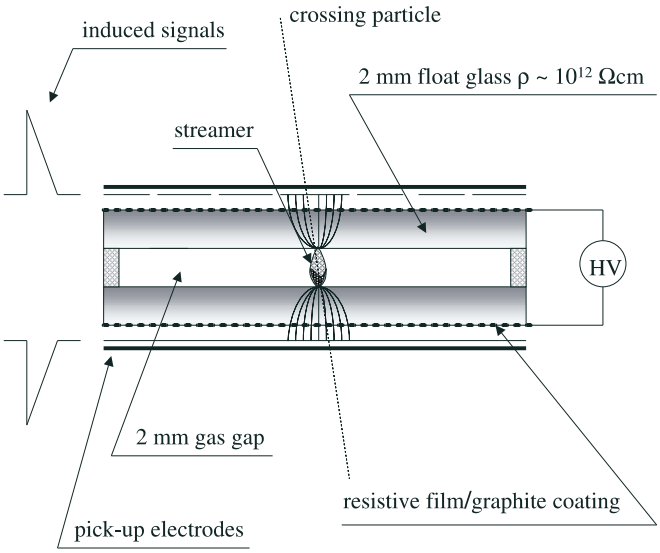

Figure 3.5: Sketch of a **G**lass **S**park **C**hamber (GSC): a crossing particle induces a spark between the 2 mm thick glass electrodes charged by the graphite coating. The gap is flushed with a gas mixture to ensure spark operation. The spark signal is picked up by the electrodes outside the GSC.

A GSC is built out of two parallel 2 mm thick glass electrodes (resistivity

of 10^{12} Ωcm) which are separated by spacers. The spacers provide a constant gap of 2 mm with an accuracy of the order of 20 μm. A potential difference of $4-5\frac{\text{kV}}{\text{mm}}$ is generated between the electrodes by the application of high voltage. A graphite coating on the glass plates is used for the application of the high voltage. The GSC is a gaseous detector. Therefore, the gap is flushed with a gas mixture of 48% Argon, 48% R134A (Freon) and 4% Isobutane (quencher additive). A passing charged particle induces a cluster of primary ionization in the gas. Due to the applied high voltage, a spark develops at the position of the ionization. Because of the usage of high resistive material, the spark only discharges a limited area around the spark location. A total discharging of the chamber is prevented and the remaining area of the chamber stays active (time to recover electric field $\tau \sim \rho\epsilon$ proportional to volume resistivity and dielectric constant).

The construction of the GSC is completed by an envelope which surrounds the glass plates separated by spacers (see figure 3.6).

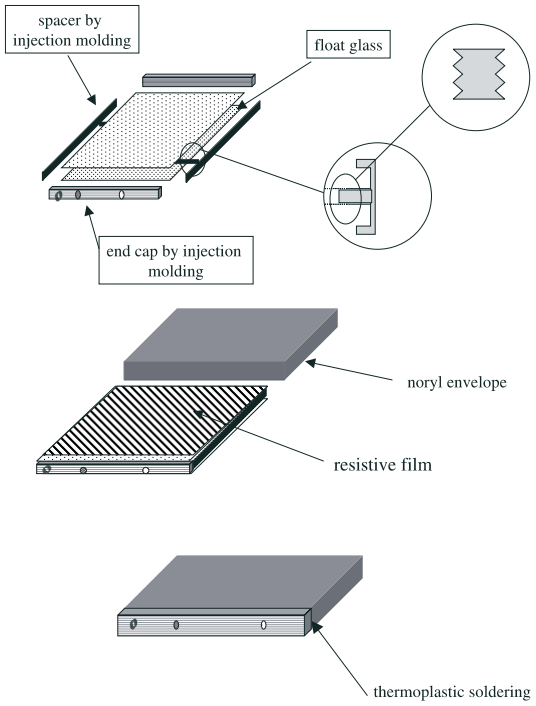

Figure 3.6: Outer design of GSC: glass plates separated by spacers are surrounded by an envelope. The envelope ensures gas tightness. In addition, the shape of the spacers is displayed which prevents surface currents and thus spark development without a passing particle.

Apart from the main function of the envelope to ensure the gas tightness of the GSC, it prevents changes in the gap distance due to increased gas pressure. A change in the distance between the glass plates has a great influence on the chamber performance. If the gas pressure increases, the volume of the gas in the GSC increases. To avoid the change of the gap distance due to the increased gas amount, the envelope can inflate and provide an extra volume between the envelope and the outer sides of the glass plates to compensate the increased gas volume in the GSC.

The signal of the induced spark is picked up by external electrodes which consist of commercial flat cables (see figure 3.7). It is discriminated by electronics mounted on cards [36] directly connected to the flat cable. Several conductors are merged to one readout strip to achieve a strip width of 3 cm. Also a fast discriminated signal required for timing purposes is provided by the electronics.

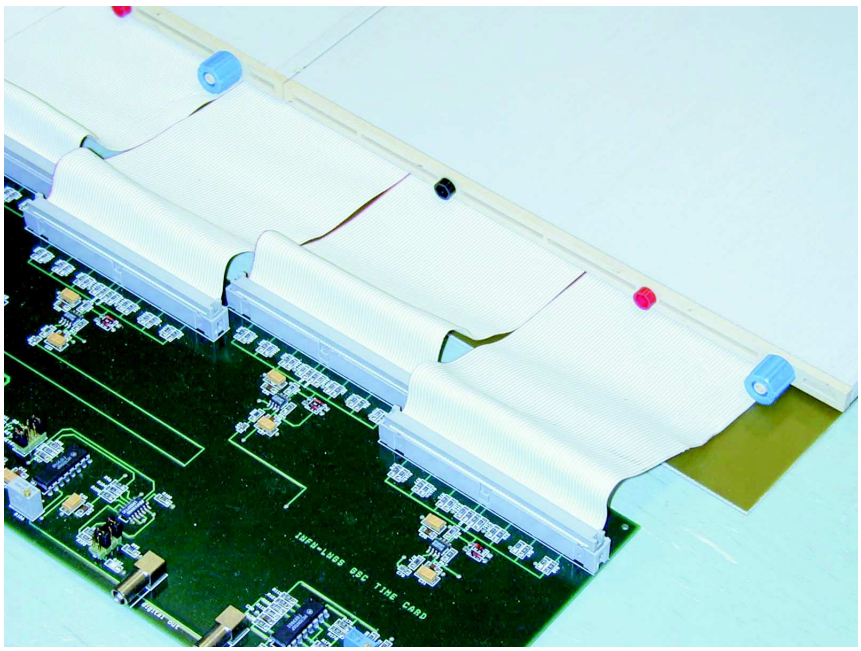

Figure 3.7: Picture of the end of a GSC with flat cables as pickup electrodes beneath. A discriminating electronic card merges several flat cable conductors to one readout strip. The provided pitch is 3 cm.

The chamber is covered with flat cable consisting of one strip layer on top and one strip layer oriented orthogonal to the first below the chamber. A passing particle induces a signal in both strip layers. In the ideal scenario, a readout strip from the top flat cable layer gives the hit information for one

coordinate, a readout strip from the bottom layer the hit information from the other coordinate. Therefore, a single chamber gives a two dimensional hit pattern for a passing particle. Taking the different layer information into account, a three dimensional tracking of particles with a time resolution of about 2 ns and a spatial resolution of about 1 cm can be provided with this design [9] (for further investigations see 4).

3.2.3 Detector Construction

The advantage of the detector design including the usage of GSC is the possible decoupling of iron structure assembly and detector insertion. The general structure divides the detector into 16 roads in the **Y** coordinate for insertion of the detector components along the **X** coordinate. 8 plate units consisting of 6 GSCs are inserted in each road (see figure 3.8).

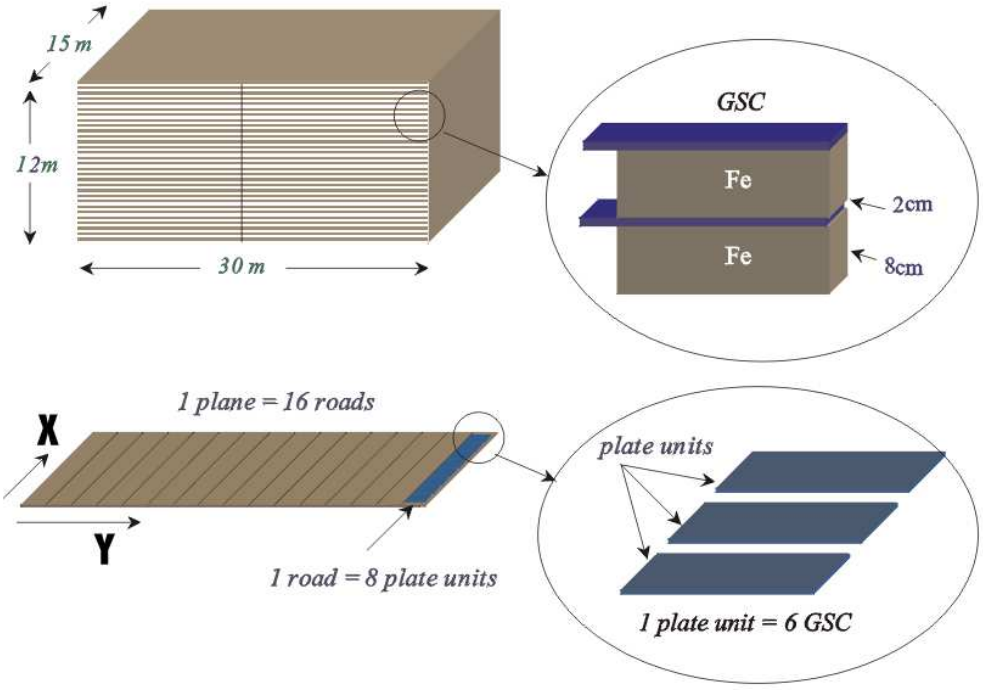

Figure 3.8: The detector is divided up into 16 roads in the **Y** coordinate for insertion of the detector components along the **X** coordinate. 8 plate units consisting of 6 GSCs are inserted in each road. In addition, a sketch of two iron layers and two active layers is displayed.

The arrangement and the readout of the strips to achieve the two dimensional hit pattern in a layer can not consist of continuous readout strips. The iron support structure of the different layers (further described in 5.5.3) consists of iron columns parallel to the **X** coordinate. These columns disturb the continuity of the **X** coordinate hit information strips. Several different designs to achieve a homogenous three dimensional hit pattern are under investigation. The design presented in the following is used in the trigger development (see 5).

The **Y** coordinate hit information is picked up by 15 m long and 3 cm wide readout strips (which stretch from one side of the detector to the other side continuously in **X** (see fig 3.9)). The signals are processed via electronics cards outside the detector.

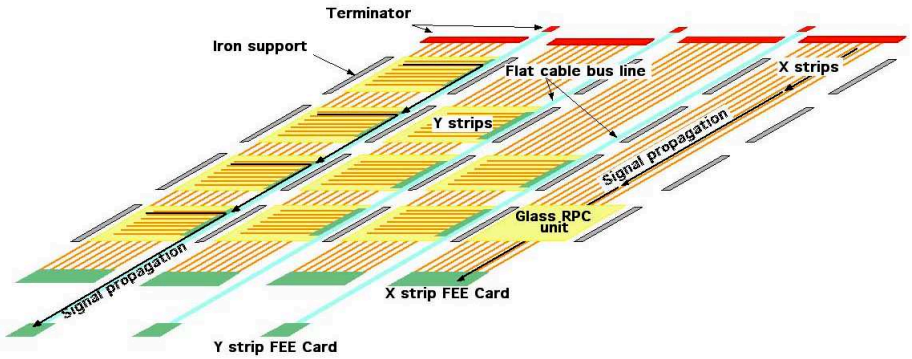

Figure 3.9: **Y** coordinate hit information (due to a different orientation labeled as X strips): read out by long readout strips with electronics outside the detector, **X** coordinate hit information (Y strips): read out by strip plates of the size of a plate unit with electronics inside the detector. The signals are merged to the **X** coordinate hit information outside the detector.

The readout strips for the **X** coordinate hit information are arranged in plates of the size of a plate unit. The merging of several flat cable conductors to a readout strip is carried out by electronics inside the detector. The readout strip signal is transported to the outside, where the signals can be combined as if a long readout strip existed.

In the most simple three dimensional geometry without a support structure and dead zones due to the mechanical design, the hit information of a single layer is represented by **1000** readout channels in **Y** and **500** channels in **X** (see example event in figure 3.10).

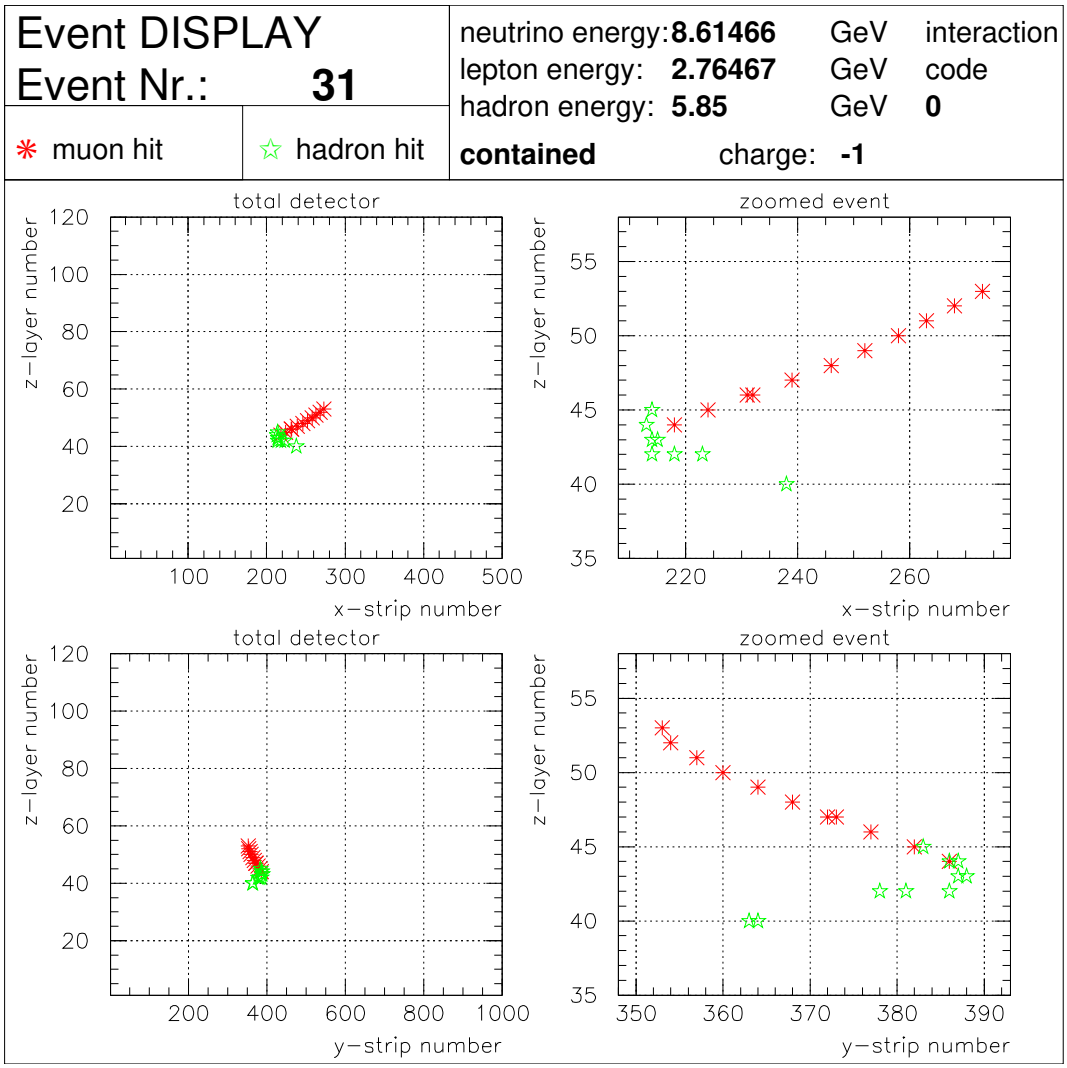

Figure 3.10: Example event display which presents **1000** readout channels in **Y** and **500** channels in **X**. Displayed are two projections of the three-dimensional detector geometry. The upper half presents the **X**-**Z**-projection including a complete and a zoomed event pattern, the lower half the corresponding **Y**-**Z**-projection. A further description of this event display is given in 5.5.5.

Chapter 4

Test Setup

For investigation of the long term performance of the main active detector component of MONOLITH, a test setup of a single GSC is built up from scratch. The work represents the practical part of the presented diploma thesis.

After an introduction to the goals of the test setup (see 4.1), a short description of the used cosmics trigger system is given (see 4.2). The single GSC setup is described (see 4.3) and the data acquisition is presented (see 4.4). In the end, a status report of the results of the still ongoing long term test is given (see 4.5).

4.1 Goals

The goals of the MONOLITH project (see 3.1.1) define certain performance requirements of the MONOLITH detector (see 3.2.1). Amongst other things, the detector has to provide for each event a three dimensional hit pattern including timing information for every hit (see 3.2.3). The stability and accuracy of these measurements have to be maintained over several years of operation.

The performance requirements of the detector have to be fulfilled mainly by the main active detector component (see 3.2.2). In the following, a test setup of a single GSC is presented. The main goal is to perform a long term test to investigate the stability of the performance of the GSC. Several test of the GSC were done by the MONLITH collaboration [9] but this specific test was not done before.

The setup of a single GSC consists of the chamber operation system (see

4.3) to investigate several chamber parameters. As a reference, a cosmics trigger (see 4.2) indicates cosmic muons (see 2.3.2) which pass the chamber.

The **main goal** is to perform a long term test. This test mainly consists of the measurement of the single hit rate of the chamber and the time between the chamber signal and the cosmics trigger reference, the time resolution. A statement of the efficiency stability over the test period can be made.

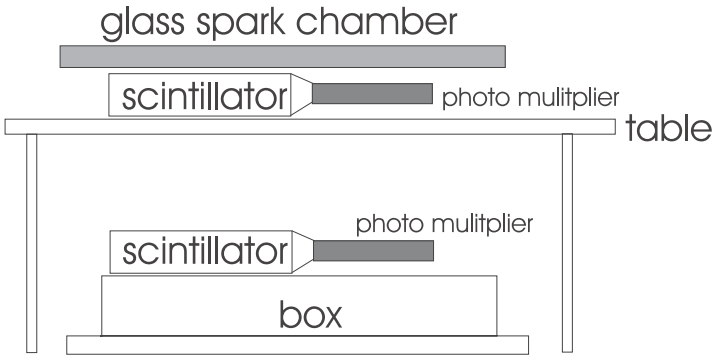

Figure 4.1: Sketch of the test setup: the cosmics trigger, consisting of two scintillator units operated in coincidence, gives a time reference for signals from the GSC, situated above.

In the following, the two main parts of the test setup (see figure 4.1), the detector part including the GSC and the support equipment for operation (see 4.3) and the cosmics trigger part also including service equipment (see 4.2) are presented.

4.2 Cosmics Trigger

The cosmics trigger is realized by scintillator units (see figure 4.1) operated in coincidence which provides a trigger for the GSC readout.

Both scintillators consist of a $50 \times 10 \times 10$ cm^3 block of plastic scintillating material connected to photomultipliers. For the operation of the photomultipliers, a complete calibration is performed (see appendix A).

The expected rate for the cosmics trigger setup can be estimated from flux predictions for atmospheric showers. An integral rate of muons (I_{int}) above $1\frac{\text{GeV}}{\text{c}}$ at the ground level of

$$I_{int} \approx 70 \frac{1}{\text{m}^2 \text{ s sr}} \tag{4.1}$$

is expected [37]. Integrated over half of a sphere of radius 1 and weighted with the angular distribution of muons at ground level ($I \propto cos^2(\theta)$), the expected rate for a horizontal detector at ground level can be derived:

$$\begin{aligned} I &= \int_{-\frac{\pi}{2}}^{\frac{\pi}{2}} \int_0^{2\pi} I_{int} cos^2(\theta)\, sin^2(\theta)\, d\theta d\phi \\ &\approx 170 \frac{Hz}{m^2} \end{aligned} \tag{4.2}$$

which leads to the expected intensity for one single scintillator of ≈ 8.5Hz. The true coincidence rate is reduced by an order of magnitude due to the strongly reduced angular coverage. An upper bound of the coincidence rate can be given by the following formula [38]:

$$\begin{aligned} I_{coinc} = 4 \Bigg\{ & L_{s_x} L_{s_z} I_{int} \alpha_x^0 \left[\frac{\alpha_z^0}{2} + \frac{1}{4} \sin(2\alpha_z^0) \right] + \\ & \frac{I_{int} d^2}{4} \ln(\cos(\alpha_x^0)) \cos(2\alpha_z^0) + \\ & L_{s_z} I_{int} d \ln(\cos(\alpha_x^0)) \left[\frac{\alpha_z^0}{2} + \frac{1}{4} \sin(2\alpha_z^0) \right] + \\ & \frac{L_{s_z} I_{int} d}{4} \alpha_x^0 \cos(2\alpha_z^0) \Bigg\} \end{aligned} \tag{4.3}$$

The formula is based on the expected cosmics rate (see equation 4.1) including the angular distribution of muons at ground level and takes the geometry of the setup (see figure 4.1) into account. The vertical distance between the centers of the scintillators is $d = 0.47$ m, the long side of a scintillator is $L_{s_z} = 0.5$ m and the short side is $L_{s_x} = 0.1$ m. The used angles are defined according to the following equations:

$$\begin{aligned} \alpha_x^0 &= \arctan\left(\frac{L_{s_x}}{d}\right) \\ \alpha_z^0 &= \arctan\left(\frac{L_{s_z}}{d}\right) \end{aligned}$$

Derived from equation 4.3, an upper bound of the coincidence is given by $I_{coinc} \approx 1$ Hz. The measured coincidence rate, which is determined in a still ongoing long term test to 0.73 ± 0.02 Hz (inclusive data taking period: 29.11.2000 to 26.01.2001) (see figure 4.2), is consistent with the expectation.

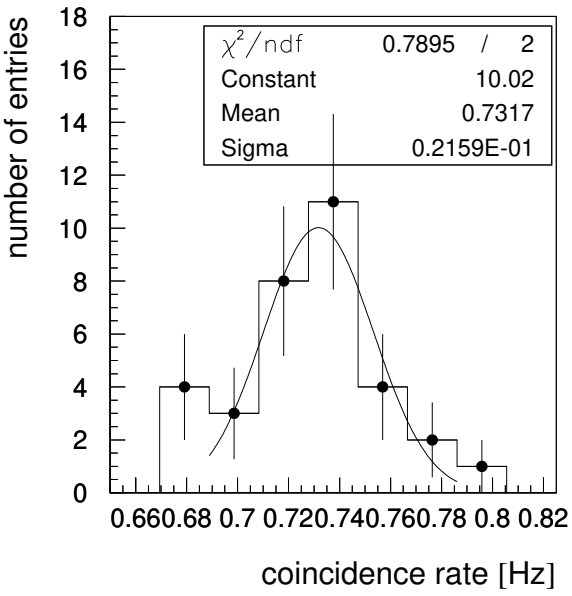

Figure 4.2: Displayed is the distribution of the measurements of the coincidence rate of the cosmics trigger obtained during the long term test (included data taking period: 29.11.2000 to 26.01.2001). The mean value of the coincidence rate is derived from a Gaussian fit.

The described cosmics trigger indicates a passing particle through the two scintillators and through the GSC. The setup of the single GSC is described in the following.

4.3 Single GSC Setup

The main part of the test setup is the single GSC ($0,25 \times 1,1$ m^2) which is situated above the cosmic trigger (see figure 4.1). The chamber and the electronics was provided by Carlo Gustavino of LNGS-INFN/ Gran Sasso. It is covered above and below with flat cables as pick-up electrodes. The signals from the flat cable conductors are fed into the electronic card (see figure 4.3) at one end of the cables. The other end is left unterminated.

The card merges the signals of the flat cable conductors to one readout signal and provides an analog and a digital output.

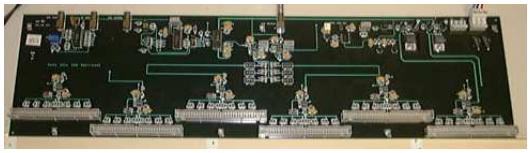

Figure 4.3: The signals from the readout strips are fed into the electronics card, which provides an analog and a digital output.

In the current setup, only the strip plane above the chamber is connected to an electronics card, the plane below the chamber is left floating. The chamber including the strips is surrounded by fiberglass sheets of which one side is copper coated. The copper coated side is orientated to the outside (see fig 4.4). Massive ground connections are soldered to the copper sides of the fiberglass sheets. The sides of the chamber which are not covered with the sheets yet are wrapped with copper tape. This completes the grounding of the chamber.

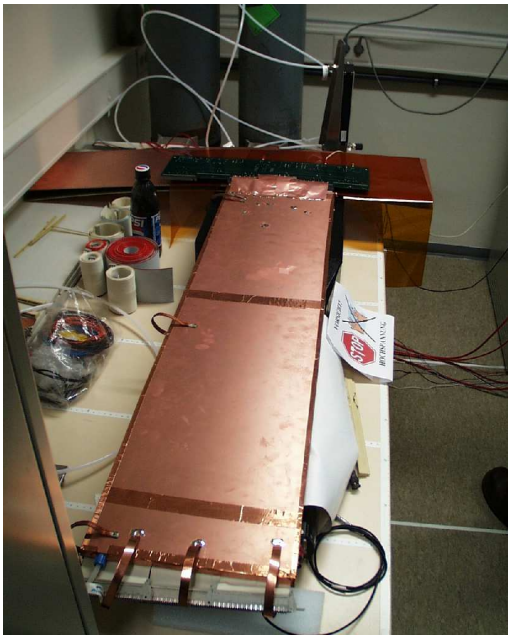

Figure 4.4: The test setup picture shows the chamber with the surrounding copper coated sheets, which are grounded by massive ground connections. The electronics card at the rear end of the chamber is connected to the sheets by several short ground connections.

The electronics card is grounded by several connections to the copper-

coated sides by the assistance of Carlo Gustavino and his team to solve reflection problems of the analog output.

The high voltage for the chamber is supplied by two high voltage supplies. One high voltage supply is charging one glass plate to 4 kV, the second charges the other plate to -4 kV to reach the required potential difference of 8 kV for a gap of 2 mm. The high voltage current does not exceed 30 μA and depends on the rate of the passing particles.

For the flushing of the chamber with the gas mixture (48% Argon, 48% R134A and 4% Isobutane), a gas supply system is realized, consisting of gas bottles, a calibrated fluxmeter (see appendix B) and an oil bubbler (see figure 4.5) providing the chamber with a gas flux of about 1 $\frac{\mathrm{l}}{\mathrm{h}}$.

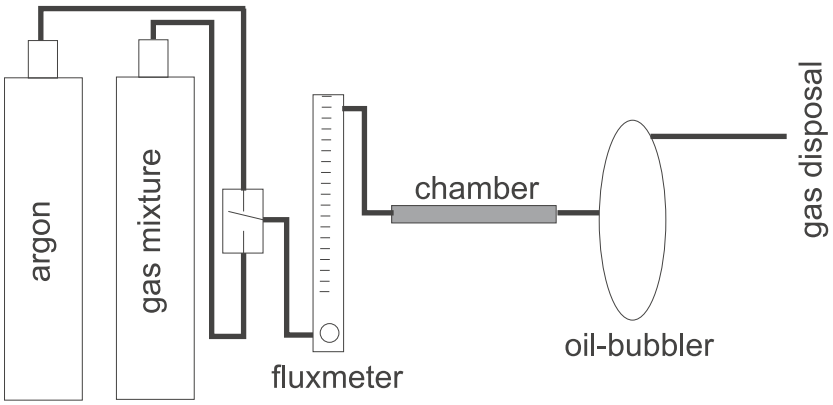

Figure 4.5: **Gas supply system**: the flux from the gas bottles is controlled by a fluxmeter and directed through the chamber and displayed by an oil-bubbler. The gas is removed through the gas disposal system. The pre-flushing with pure Argon is possible by changing the gas input at a valve.

The signals of the GSC with respect to the coincidence signals of the cosmics trigger are processed by the data acquisition.

4.4 Data Acquisition

The electronics card (see figure 4.3) provides an analog and a digital output. The output of the digital signal is triggered by an adjustable threshold on the card, which is set to 45 mV to discriminate the analog signal (see figure 4.6). This value was chosen to ensure proper operation of the chamber.

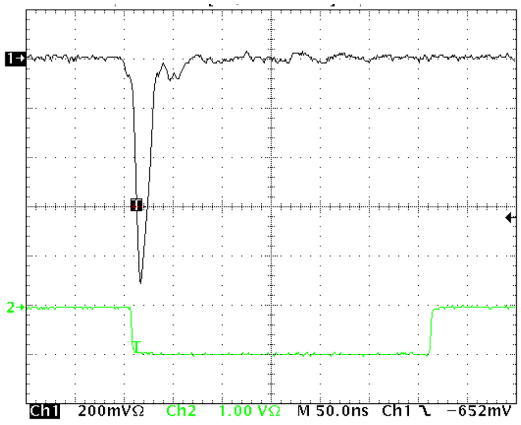

Figure 4.6: Analog (upper, scale 200 mV per division) and digital (lower, scale 1 V per division) GSC signal from electronics card (time scale 50 ns per division). The digital signal has a greater width to avoid double pulses in the measurements.

Only the digital signal is used for performing the two different measurements:

1. The **single hit rate** of the chamber is recorded by scaling the digital output. At the same time, the rate of the cosmics trigger is recorded (see figure 4.2).

2. The **time resolution** is measured with a time-to-digital (TDC) converter setup (see figure 4.7). The used VME-TDC (CAEN V488 AS) is operated in a VME crate with Motorola processor card. LynxOS is used as operating system and a C-program controls the TDC over the VME interface.

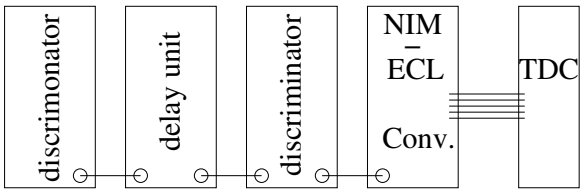

Figure 4.7: Sketch of TDC setup including NIM-to-ECL converter and delay unit.

The digital NIM signal[1] is converted to differential ECL[2] and recorded with one channel of the TDC. As a reference signal, the cosmics trigger coincidence is fed into the common input of the TDC. The conversion of NIM to ECL requires an appropriate converter. The used converter turns out to be slightly unstable and is preceded by discriminators to ensure its functionality.

The cosmic trigger coincidence is used as common start signal for the TDC. After the TDC gets the common start signal, the time is measured between the start and a signal from the GSC. The coincidence signal emerges later with reference to the GSC signal (see figure 4.8) and the latter has to be delayed with a delay unit (see figure 4.7).

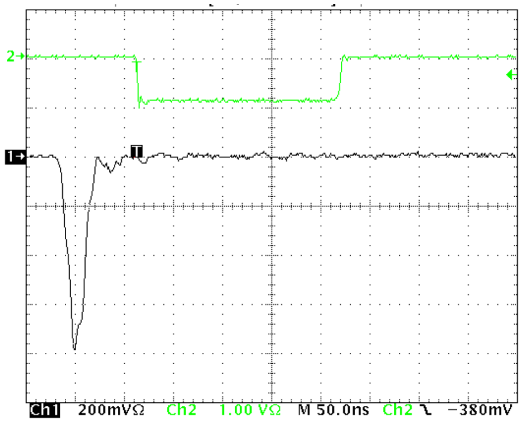

Figure 4.8: Signal of a passing particle through the chamber in reference to the cosmics trigger coincidence. Upper signal: cosmics trigger coincidence (scale 1 V per division). Lower signal: analog electronics card signal (scale 200 mV per division).

The measured shape (see fig 4.9) is fitted by a Gaussian restricted to the main pulse. Only the width of the time resolution is measured, the absolute measurement could not be performed due to the setup design. The tail at large time values originates from deviation in the electric field strength from the nominal value at positions where a spark develops [35]. The single measurements result in a mean time resolution of 2.24 ± 0.15 ns, which is

[1] Normed digital signal: logic 0 is equivalent to ± 0V, logic 1 is equivalent to -0.8V.

[2] difference of two digital signals to filter induced noise: *first signal*: logic 0 is equivalent to -0.8V, logic 1 is equivalent to -1.6V. *Second signal*: logic 0 is equivalent to -1.6V and logic 1 is equivalent to -0.8V.

consistent with the measurements of the time resolution by the MONOLITH collaboration [9].

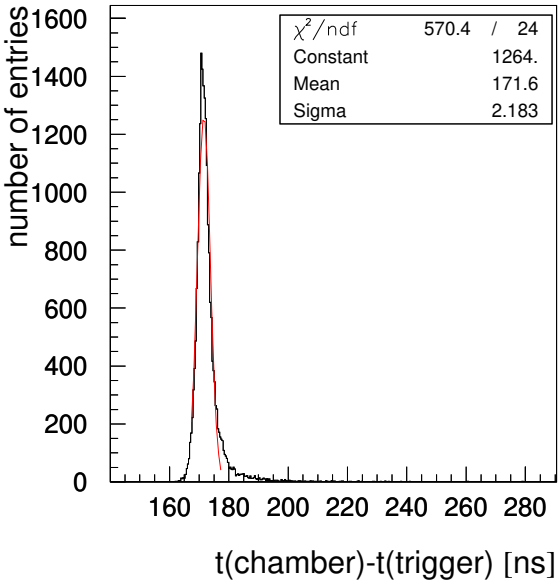

Figure 4.9: The time resolution of the chamber is the time between the response of the chamber and the cosmics trigger coincidence. An exemplary measurement presents a time resolution of a sigma of 2.18 ns.

In the following, a status report of the still ongoing long term test is presented.

4.5 Status Report of the Long Term Test

The long term test is performed with the single chamber setup. The setup is not changed during the longterm test. The presented data covers the test time from 29.11.2000 to 26.01.2001. To measure the long term stability of the chamber, several parameters are repeatedly recorded:

- The single hit rate of the chamber is measured by a 10 MHz scaler.
- The time resolution of the chamber is measured by the TDC setup.
- The cosmics trigger coincidence rate is measured by TDC setup and the scaler.

- The chamber signal rate in reference to the cosmics trigger is measured by the TDC setup.

The single hit rate investigation shows that the initially high rate stabilized during the long term test (see figure 4.10). The rate is mostly due to noise from the chamber (for instance the voltage breakthrough without passing particle) and decreases during longer operation due to the decreasing amount of gas contaminations (possible germ cell of breakthrough) of the chamber. For example, the chamber can be contaminated by air which enters the gas circuit before starting the operation. The observed rate is consistent with expectations of $\sim 500\ \frac{\mathrm{Hz}}{\mathrm{m}^2}$ from earlier short term test of the MONOLITH collaboration in Gran Sasso and at CERN.

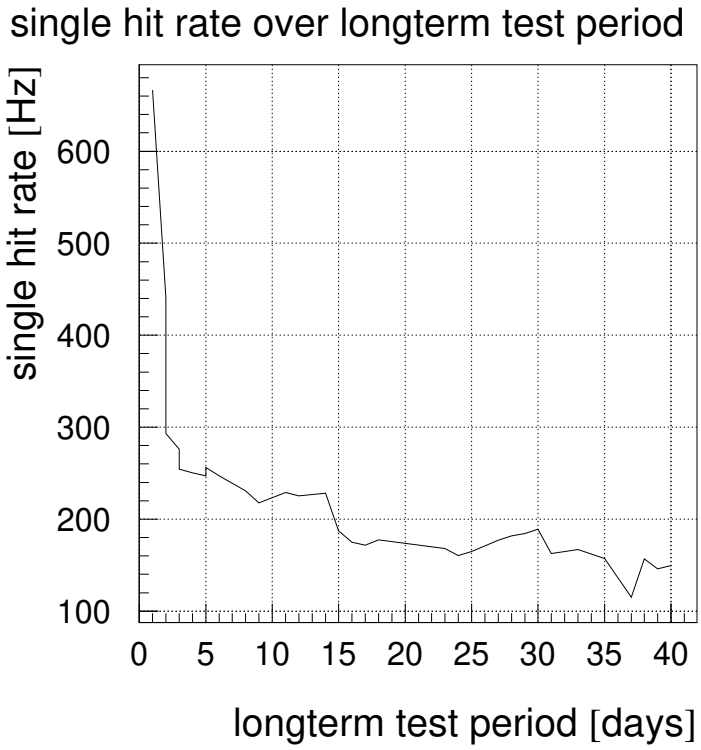

Figure 4.10: Displayed is the stabilizing effect of the chamber during operation. Shown is the decreasing of the single hit rate due to possible decreasing of chamber contamination.

Investigation of the time resolution results in the same stabilizing effect, but this time more rapidly (see figure 4.11). After this effect, the time resolution shows a more or less constant behavior.

The statistical errors are small with respect to the systematic errors. The systematic fluctuations are of the order of about 20%. The frequent change of the gas bottles and the contamination due to the change operations are possible sources of systematic errors apart from possible influences of the setup.

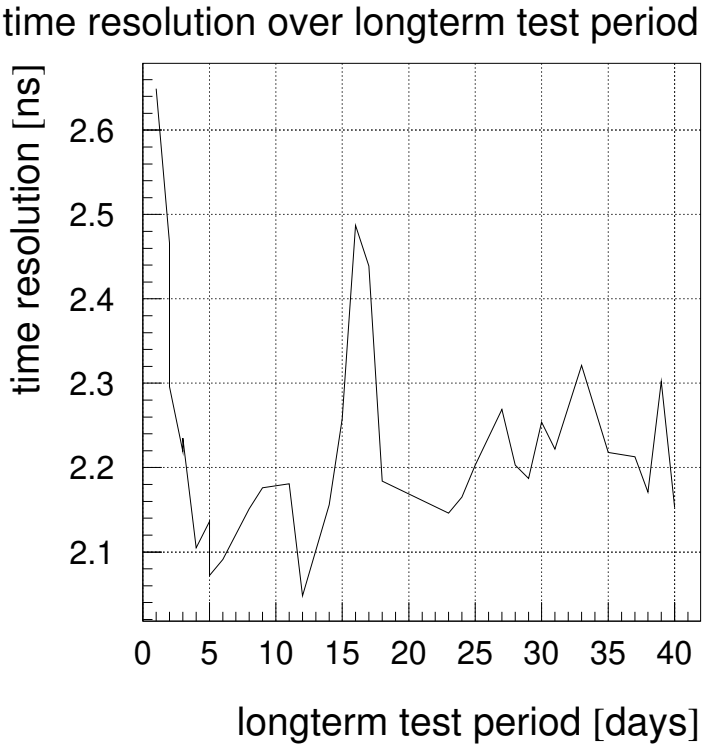

Figure 4.11: The time resolution stabilizes during operation and remains constant. Explanation can be given by decreasing of contaminations.

The efficiency of the chamber, indicated by the ratio of the processed TDC signals to the cosmics trigger coincidences (see equation 4.4),

$$\mathcal{E} = \frac{\mathcal{R}_{\text{processed TDC signals}}}{\mathcal{R}_{\text{cosmics trigger coincidences at TDC}}} \tag{4.4}$$

shows also a short stabilizing effect (see figure 4.12) but remains almost constant afterwards. The resulting efficiency is smaller than the measured chamber efficiency by the MONOLITH collaboration [9] due to the selected threshold on the electronic card and influences from the setup. The threshold is fixed to a reasonable value (see 4.4) to ensure proper operation.

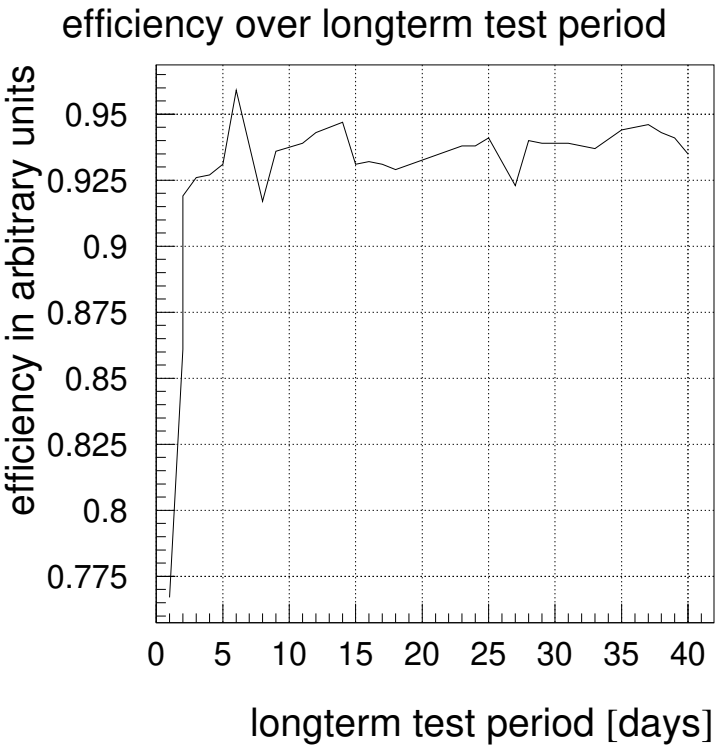

Figure 4.12: Efficiency as the ratio of processed TDC signals to cosmics trigger coincidences shows a stabilizing effect due to the decreasing of contamination and afterwards shows an almost constant behavior.

The long term test so far indicates the stability of the chamber efficiency within systematic fluctuations of about 6%. It presents the longest test of the GSC so far and still continues.

Chapter 5

Trigger Development

The development of the trigger for the MONOLITH project represents the main goal of this thesis. In the following, the different steps of the development process are presented. In the beginning, a description of the basics of a trigger in general and in the context of the MONOLITH project (see 5.1) is given. The trigger rate, one of the considered performance criteria of the MONOLITH trigger, is explained and its components are discussed (see 5.2). The structural design of the trigger algorithm is presented (see 5.3) and the data sources which are used for the trigger investigation are described (see 5.4). The data processing of the described data sources including several event displays (see 5.5) is described. In the end, the optimization of the trigger is presented (see 5.6).

5.1 Basics of a Trigger

In general, a trigger "separates the wheat from the straw".

For example, the cosmics trigger of the test setup (see 4.2) separates the signals of the GSC which belong to passing muons from all other GSC signals. The trigger uses the scintillator coincidence as an external information source for the separation. If the scintillator coincidence signal and a signal from the GSC appear in coincidence, it is most probable that the signal from the GSC was induced by a passing muon.

For the MONOLITH project, the concept of a trigger has to be adopted in a different way. The MONOLITH project is designed to prove atmospheric neutrino oscillation (see 3) by exploiting the ν_μ disappearance method (see 2). Therefore, it has to detect the charged final states of the neutrino interactions. This is done amongst other things by combining the three dimensional hit pattern of the MONOLITH detector to tracks of the different final

states. The MONOLITH trigger has to distinguish the hit pattern resulting from neutrino interactions from other hit patterns which do not contribute to the goals of MONOLITH (see 3.1.1). In contrast to the cosmics trigger, the MONOLITH trigger uses the hit pattern itself and not an external source for the distinction. The MONOLITH trigger presented in the following is planned to be directly implemented by hardware.

For performance investigations concerning the MONOLITH trigger, two criteria are regarded in this thesis. The efficiency is defined as the ratio of the events actually selected by the MONOLITH trigger to the total number of events which the MONOLITH trigger is intended to select. Furthermore, the trigger rate which indicates how often the MONOLITH trigger finds potentially useful events per unit of time is considered (for a detailed discussion see 5.2).

The MONOLITH trigger has to fulfill several requirements:

1. Due to the small cross section of neutrino interactions (see 2.1.1) in combination with the atmospheric neutrino flux, the rate of neutrino events is very small compared to other events in the detector (further explained in 5.2). A high efficiency reduces the time to gain sufficient statistics for the analysis. Therefore, the efficiency should be close to 1. The efficiency indicates how many neutrino interactions are selected by the MONOLITH trigger with respect to all neutrino interactions in the MONOLITH detector.

2. To reduce costs, the electronics effort of the trigger should be as minimal as possible without compromising the trigger performance.

3. The trigger rate has a large impact on the data acquisition (not further explained). For the presented investigation, an overall trigger rate limitation to **1 kHz** is assumed which is an acceptable rate for a consecutive processing.

The efficiency and the trigger rate represent criteria to investigate the performance of the MONOLITH trigger according to the defined requirements. The efficiency of the MONOLITH trigger is determined by the application of the trigger to a Monte Carlo simulated event sample (see 5.4.1) whereas the investigation of the trigger rate requires a discussion of the components of the trigger rate.

5.2 Components of the Trigger Rate

The hit pattern is composed out of the hits recorded in a certain time which is called trigger time. There are several sources of hit patterns which contribute to the trigger rate.

Three main sources of hit patterns contribute to the expected trigger rate and are treated separately:

- The hit pattern which originates from neutrino interactions in the MONOLITH detector (see 3.1.1) (in the following quoted as physics events).
- The hit pattern from background events consisting of muons of the cosmic radiation (see 2.3.2) which generate a hit pattern which is similar to the physics events.
- Random hits from the noise hit rate of the GSC can also create hit patterns similar to the patterns of physics and background events. These patterns again contribute to the trigger rate.

5.2.1 Neutrino Events

The most important source of hit pattern in the detector with respect to the goals of MONOLITH is represented by the neutrino interactions in the detector. The simulations which determine the detector performance [9] result in about **2500** expected neutrino events with $E_\nu > 1$ GeV corresponding to a measurement of one year with a 34 kt detector. This corresponds to a neutrino event rate for the MONOLITH detector of

$$I_\nu = 8 \cdot 10^{-5} \text{ Hz} \tag{5.1}$$

Due to the requirement of a high efficiency of the MONOLITH trigger close to 1, the expected neutrino event rate is essentially equal to the expected trigger rate contribution from the neutrino events.

5.2.2 Cosmic Muon Background

The background resulting from cosmic ray muons in underground laboratories as a function of rock depth has been under investigation for a long time. The results for the Gran Sasso underground laboratory are given by the MACRO collaboration [39] and the LVD collaboration [40] and a flux of $4 \cdot 10^6$ muons per year is expected for a detector of the base size of MONOLITH. The corresponding rate is

$$\begin{aligned} I_{\text{cosmic}} &= 1 \frac{1}{\text{hour m}^2} \times (15 \times 30)\,\text{m}^2 \\ &= 0.13 \text{ Hz} \end{aligned} \tag{5.2}$$

which is directly taken as the trigger rate contribution of cosmic muons since long muon tracks will obviously satisfy the trigger condition described below.

5.2.3 GSC Single Hit Rate

The bigger contribution to the trigger rate originates from the noise of the GSC (see figure 4.10). The long-term test (see 4.5) results in a single hit rate of about 160 Hz per test chamber. After rescaling based on the test chamber size ($0,25 \times 1,1$ m^2), a noise rate of about

$$I_{\text{noise}} = 580 \frac{\text{Hz}}{\text{m}^2} \tag{5.3}$$

is expected.

With the total active detector area (see 3.2.1) of about 54000 m^2 a total noise rate of about **31 MHz** is estimated if every hit is taken into account.

Resulting from the investigation of the different sources which contribute to the trigger rate, a significant influence from neutrino and cosmic muon events to the trigger rate is not expected. Therefore, the trigger rate is dominated by the single hit rate of the GSC.

In the next section, the structural design of the investigated MONOLITH trigger algorithm based on the defined requirements is explained.

5.3 Design of the Trigger Algorithm

The functionality of the MONOLITH trigger is described to present the structural design of the investigated trigger.

The trigger investigates the hit pattern recorded over the trigger time. The intention of the MONOLITH trigger to determine whether the corresponding event originates from a neutrino interaction and has to be recorded by the data acquisition or not is carried out by the application of the trigger algorithm to the hit pattern. The trigger algorithm represents the logical implementation of the MONOLITH trigger and defines the trigger condition which has to be fulfilled by the hit pattern. A trigger condition indicating

a neutrino event results in the output of a trigger signal which initiates the recording of the event by the data acquisition.

If the MONOLITH trigger would be applied to the complete three dimensional hit pattern (see figure 3.10) recorded over the trigger time, the decision process would be very complicated due to the great amount of data which has to be investigated. Amongst other things, the process would take too much time and/or would contradict the requirement of minimal electronics effort. In order to achieve cost and hardware expense reduction, the complete detector response (see 3.2.3) should be intensely reduced and simplified before being used for triggering purposes. The basic strategy consists in the limitation of the three dimensional hit pattern of the MONOLITH detector (see 3.2.3) to a reduced two dimensional pattern. This is done by considering only the **Y** hit information plane. The hit pattern of originally 1000 strips per layer is merged by means of the introduced road structure (see 3.2.3). In each road, all channels of each layer are merged into a single trigger channel. This results in a hit pattern of 16 **trigger channels** per layer or overall 1920 **trigger channels** (see figure 5.1).

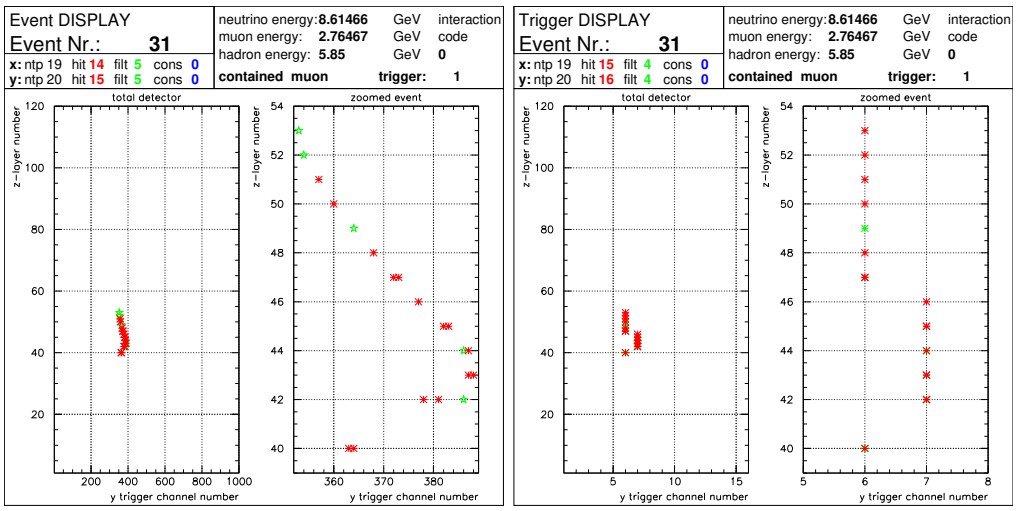

Figure 5.1: The **Y** coordinate hit information pattern (*left*) is reduced to the trigger pattern (*right*) consisting of 16 trigger channels per layer or overall 1920 trigger channels. The shown displays are explained in detail in 5.5.5.

The full hit pattern of a neutrino interaction still shows a certain structure after the reduction to the trigger pattern. The track transforms to clusters of hits in individual roads. This characteristic can be used to distinguish hit patterns of neutrino interactions from other hit patterns.

For further reduction of the effort, the trigger is not applied to the complete trigger pattern but to different parts called **units**. The units are constrained to individual roads and therefore consist of consecutive trigger channels which are in the same road but in different layers. In addition, the units are situated in the roads with a certain number of layers of overlap. The trigger condition requires a certain number of trigger hits in a unit to decide whether the investigated pattern originates from a neutrino interaction or not (see figure 5.2).

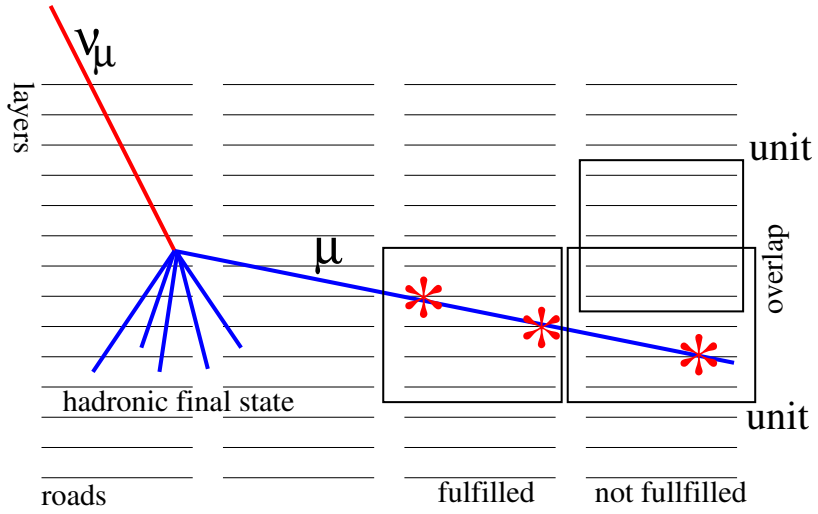

Figure 5.2: Example implementation of the MONOLITH trigger: the final states of the neutrino interaction generate trigger hits. The investigated unit of a size of 5 layers includes 1 hit in one road and 2 hits in another road. In the case of two required hits in a unit , the event fulfills the trigger condition.

The hardware implementation of the trigger algorithm constrains the possible number of consecutive layers in a unit to less than 6. The trigger algorithm is planned to be realized by VME-triggerboards which process the trigger channels by local logic-circuits. These boards allow the implementation of the described trigger algorithm design.

In the following, the optimization of the MONOLITH trigger with respect to the efficiency and the trigger rate is presented according to the variation of the **three parameters** of the MONOLITH trigger algorithm:

1. The number of consecutive layers per unit (**UNIT**).

2. The number of layer overlap between adjacent units (**OVERLAP**).

3. The number of required hits in a unit (**HIT**).

In addition, the trigger time and the single hit rate of the GSC have an impact on the presented investigation.

As derived from the discussion of the different components of the trigger rate (see 5.2), a trigger rate of 31 MHz has to be expected if every hit is taken into account. This rate is not compatible with the defined requirement of < 1 kHz. As a preliminary starting point, the trigger rate of a loose parameter combination is investigated. For this the rate per trigger channel is needed. This rate can be estimated from the detector area of a road per layer and the single hit rate of the GSC (see equation 5.3):

$$\begin{aligned} I_{\text{road}} &= 15\text{m} \times 1,8\text{m} \times 580\frac{\text{Hz}}{\text{m}^2} \\ &= 15,7\text{kHz} \end{aligned} \tag{5.4}$$

As a starting point, a statistical investigation of a soft trigger parameter combination of a 5 layer wide unit of consecutive layers (UNIT=5) and 2 required hits in a unit (HIT=2) is performed. The overlap is set to 4 and its effect can therefore be neglected. Starting from a given trigger hit in the detector, a second hit has 8 possibilities to fulfill the trigger condition. Using a trigger time of 100 ns, which represents a particle traveling at speed of light the 30 m baseline of the detector, and considering the 1920 trigger channels for the trigger hit, the trigger rate can be estimated (see equation 5.5). It is assumed that the signal transit time and the processing time in the hardware are the same for all trigger channels. The described design fulfills this assumption.

$$\begin{aligned} I_{\text{UNIT=5,HIT=2}} &= 15,6\text{kHz} \times 8 \times 15,6\text{kHz} \times 100\text{ns} \times 1920 \\ &= 376,5\text{kHz} \end{aligned} \tag{5.5}$$

This high rate is incompatible with the required trigger rate of less than 1 kHz. A higher number for the required hits in the unit (HIT) is therefore required to fulfill the restriction of the trigger rate. A detailed investigation is presented after the description of the used data sources.

5.4 Data sources

For further investigation of the different trigger parameter combinations, two sources of events are used. The efficiency of a combination is investigated

using an event sample generated with the MONOLITH Monte Carlo simulation (see 5.4.1 and [9]), which is further referred to as the neutrino sample. For the trigger rate investigation, a separate simulation is performed which generates noise events according to the single hit rate of the GSC (see figure 4.10). The resulting event sample is further referred to as the noise sample.

5.4.1 Monte Carlo Generated Events

For the simulation of neutrino events in the MONOLITH detector, information about the atmospheric neutrino flux at the underground laboratory in Gran Sasso is needed. The differential distribution of the atmospheric neutrino flux is given by the Bartol model [41]. The distribution of the production height of the neutrino in the atmosphere is described by calculations of Gaisser and Stanev [42]. The interactions of the neutrinos in the detector are calculated with GRV94 parton distributions [43] and include the contributions of quasi-elastic scattering and single pion production to the neutrino cross-section [44]. The detector structure is simulated using the GEANT package [45].

The neutrino sample is provided by T. Tabarelli and F. Terranova of the MONOLITH collaboration and consists of overall 63846 events with $E_\nu > 1$ GeV. For each event, the following event properties are provided:

1. the momenta of the neutrino, the muon and the hadronic components at generation in GeV,
2. the vertex coordinates in cm, according to a reference system with the geometrical center of the detector as origin,
3. the corresponding neutrino interaction category (for example NC or CC) given by the interaction code,
4. the charge of the muon,
5. a flag whether the muon is contained in the detector volume or outgoing.

The hit information of the event is given separately for the **X** and **Y** coordinate and each hit information consists of the following properties:

1. the number of the strip according to the hit pattern in the **X** or **Y** coordinate,

2. the number of the layer,

3. the information whether the hit is produced by a muon or by a hadron,

4. the time-of-flight information.

The detector simulation is based on the presented detector design (see 3.2.3) and simulates 500 read-out strips in **X**, 1000 read-out strips in **Y** and 120 layers with active detector components in **Z**. The readout strips continously cover an individual layer. Therefore, the simulation for the resulting neutrino sample does not yet contain information about **dead zones** of the detector, which have to be introduced (see 5.5.3).

The neutrino energy is directly derived from the given neutrino momentum whereas the muon energy is calculated with the given muon momentum by taking the muon mass into account. The hadron energy is determined as difference of neutrino and muon energy under the assumption of energy conservation. The neutrino energies of the events of the sample have values between 1 GeV and 3691 GeV, the muon energies between 100 MeV and 2944 GeV and the hadronic final state between 0 GeV and 1764 GeV (see figure 5.3).

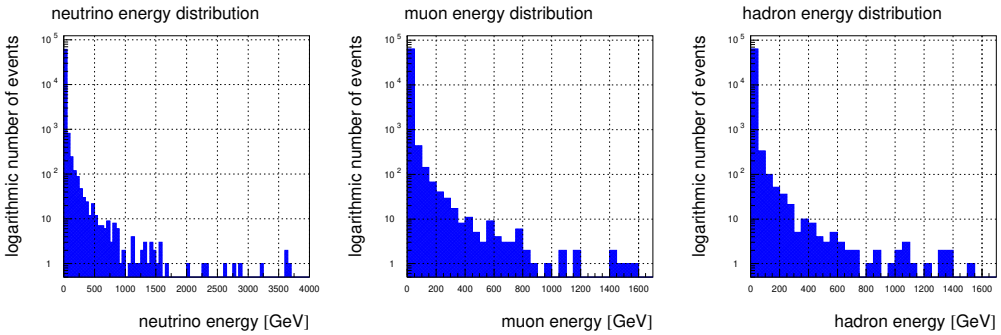

Figure 5.3: Energy distribution of the neutrinos (left column), the muons (center column) and the hadronic final state (right column) of the neutrino sample.

In the generation of the neutrino sample, a cut on a fiducial detector volume was included. Due to the chosen geometrical reference system, the **x** coordinate of the vertex can be found within the range of -750 cm to 750 cm, the **y** coordinate in the range of -1500 cm to 1500 cm and the **z** coordinate in the range of -600 cm to 600 cm. As can be seen from the distribution of the vertex coordinates (see figure 5.4), simulated events with a vertex in

the outermost 5 *read-out strips* of the **X** and **Y** coordinate or respective the outermost 15 cm of the **x** or **y** coordinate of the vertex position are not included in the neutrino sample. In the **z** coordinate (the layer number), events with a vertex position in the outermost 4 layers or 36 cm are left out of the sample. This selection corresponds to a fiducial volume of 31 kt.

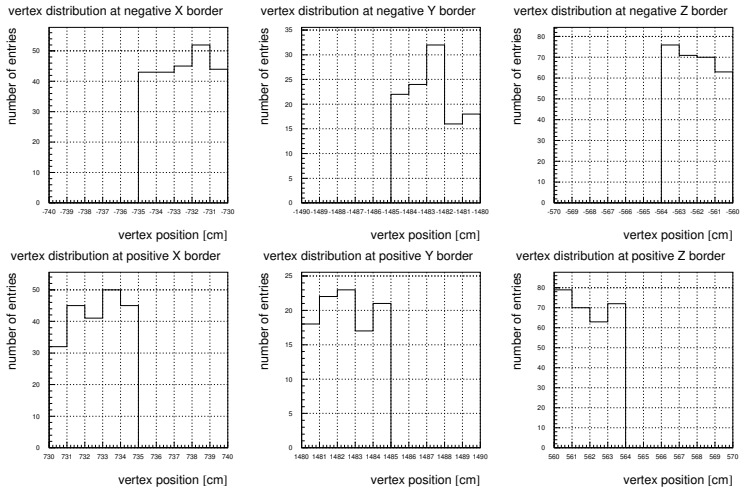

Figure 5.4: Vertex distribution in cm for the **x** coordinate (left column), the **y** coordinate (center column) and the the **z** coordinate (right column) in a reference system with the geometrical center of the detector as origin.

5.4.2 Noise Simulation

The noise of the GSC given by the single hit rate is identified to be the main contribution to the trigger rate (see 5.2). To investigate the influence of the variation of the trigger parameter combinations, a noise simulation is performed to generate a noise sample similar to the neutrino sample (see 5.4.1).

This simulation was specifically written for the purpose of this thesis. It is based on the single hit rate investigation of the long term test (see figure 4.10) and takes the measured rate scaled to the test chamber size as input:

$$I_{\text{single hit rate}} = 580 \frac{\text{Hz}}{\text{m}^2} \tag{5.6}$$

which results in the single hit rate of the detector:

$$\begin{aligned} I_{\text{detector}} &= 580\frac{\text{Hz}}{\text{m}^2} \cdot (15\text{m} \times 30\text{m} \times 120\text{layers}) \\ &\approx 31\text{MHz} \end{aligned} \tag{5.7}$$

In general, the noise simulation generates hits in the detector. These hits are distributed randomly in space and time. The generated hits are then ordered according to increasing time. To preselect events, the trigger algorithm of a loose trigger parameter combination is applied to the generated hits. If the trigger condition is fulfilled, the hits in a defined time range in reference to the hits belonging to the fulfilled trigger condition are combined to an event, and only such events are written out to reduce the data space consumption.

The noise simulation algorithm consists of two parts, the **generation** and the **trigger** part.

In the generation part, a **millisecond** is randomly filled with hits according to the expected single hit rate. The millisecond is divided up into intervals of the length of one microsecond. In each microsecond, a random number of hits according to a Gaussian distribution is generated. As mean value of the distribution, the number of hits in one microsecond according to the single hit rate (see equation 5.7) $\mu = 31\ \text{MHz} \cdot 1\ \mu\text{s} = 31$ is chosen. The standard deviation is determined by the square-root of the mean value: $\sigma = \sqrt{\mu} = 5.57$, whereas the distribution is constrained to non-negative values in a 6σ range around the mean value. Only the **Y** hit information is simulated since the trigger uses only the **Y** hit information. For each hit, the road information (range: 1 to 16), the layer information (range: 1 to 120) and the time information (range: 0 to 1000 ns) are obtained from flat distributions. The layer information is transformed to a strip information by replacing the road number with the strip number in the center of the road. The hits in the microsecond are sorted according to increasing time. The different microsecond intervals are combined to the millisecond presample.

In the trigger part, the loose parameter trigger combination is given by 2 required hits (HIT=2) in a 5 layer wide unit (UNIT=5) at an overlap of 4 layers (OVERLAP=4) with a trigger time of 100 ns. If the trigger condition is fulfilled, an event is stored with all hits in a 100 ns time range in reference to the first hit of the fulfilled trigger condition (see figure 5.5).

The estimated trigger rate of the loose combination of trigger parameters (see 5.3) is incompatible with the requirement of a trigger rate of less than 1 kHz. The number of required hits has to be increased to decrease the trigger rate. Combinations with a higher required hit number can be applied

directly to the resulting events from the loose parameter combination trigger application.

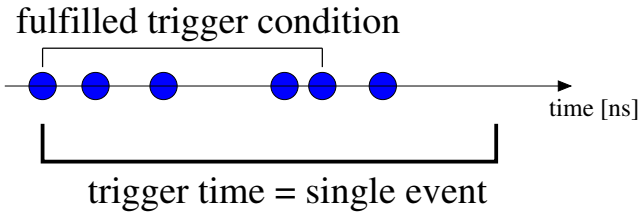

Figure 5.5: The trigger procedure of 2 hits (HIT=2) in 5 layers (UNIT=5) stores event of 100 ns time spread when the trigger condition in the presample is fulfilled.

The required statistics is obtained by repetition of the described noise simulation. The simulated time range is 1 second which results in a number of events which is comparable to the neutrino sample.

The generated events are stored in a format equal to the neutrino sample format. The two event samples are now investigated using the same data processing procedures.

5.5 Data Processing

The **data processing** is performed for both event sources in the same way. It consists of several stages which are applied to each event in the presented order.

1. The **read procedure** (see 5.5.1) gets all information of the event from the event sample and stores them in variables.

2. The **cut procedure** (see 5.5.2) sets cut flags if the event fulfills cuts corresponding to the atmospheric neutrino oscillation pattern analysis cuts [9].

3. The Monte Carlo event generation (see 5.4.1) does not include dead zones in the detector. The hits which are geometrically situated in a dead zone are marked by the **dead zone procedure** (see 5.5.3) and are not included in the analysis.

4. The **trigger procedure** (see 5.5.4) determines whether the event fulfills defined trigger parameter combinations and sets trigger flags for each investigated combination.

In the end, an additional data file consisting of the event information and the results of the processing stages is created for each event source. After the discussion of the different data processing stages, several event displays (see 5.5.5) used for visualization of the data processing are described.

5.5.1 Read Procedure

The read procedure provides all following procedures with the complete event information stored in variables according to the event structure from the Monte Carlo event sample (see 5.4.1). Apart from the hit information for the three dimensional hit pattern separated into muon and hadronic hits, the energies for the neutrino, the muon and the hadronic final state are stored. The interaction code of the generated neutrino interaction and the charge of the muon are stored and a flag indicating whether the muon is outgoing or contained in the detector volume is generated. In addition, the vertex coordinates are stored. The visualization of the read procedure is given by the event display, which is further explained in 5.5.5.

5.5.2 Oscillation Analysis Cuts

The direct observation of the atmospheric neutrino oscillation pattern requires a pure ν_μ-CC event sample with "high resolution" in $\frac{L}{E}$ [9]. Several cuts were applied to fulfill this requirement:

1. A muon energy of at least $1,5$ GeV is required to obtain a pure ν_μ-CC event sample.

2. Muons which stop in the detector (contained events) have to be included in a fiducial volume, which requires events with no hits in the outermost 10 read-out strips in the **X** and **Y** direction and in the outermost 4 layers.

3. The track length of outgoing muons is required to be at least 4m to guarantee the rejection of the cosmic muon background.

4. The muon track has to cover at least 7 layers.

The combination of the required cuts reduces the detector volume to a fiducial volume of 26 kt comparable to the fiducial volume of the Super-Kamiokande detector (see 2.4).

5.5.3 Dead Zones

To take the neglected dead zones of the detector in the event generation (see 5.4.1) into account, the hits situated in a dead zone are marked and are not included in the analysis. Therefore, the dead zones, which are given by their position in the detector, have to be translated into strip numbers which are equivalent to the strip pattern of the neutrino sample (see 5.4.1). This is done by calculation of the equivalent strip position of the dead zones.

The tagging of a hit in a dead zone is performed separately for each hit of an event. The position of the hit is compared to the strip positions of the dead zones. If the hit is situated in a dead zone, the dead zone procedure marks the hit and continues with the next hit of the event. If no agreement of the hit and a dead zone can be found, the hit is marked valid and the investigation of the next hit of the event is started.

The hit information of the **X** and **Y** directions is given separately. The two directions are treated separately by the dead zone procedure although only the **Y** hit information is required for the trigger (see 5.3). The **X** hit information is prepared for the trigger investigation to make the investigation of a trigger possible which takes only the **X** hit information into account.

The dead zone treatment is not independent for the **X** and **Y** hit information. A passing particle induces a signal on both sides of the chamber and therefore a consistent hit in both coordinates. If a hit in the **Y** direction is situated in a dead zone and it is marked by the dead zone procedure, a corresponding hit in the **X** direction has to be marked as well. Also the corresponding case of a marked hit in the **X** direction has to be considered. Consistency checks take care of these requirements.

The dead zones fall into two categories, the dead zones corresponding to the coarse support structure of the iron layer support and the dead zones due to the fine structure of the GSC.

Dead zones with respect to the implementation of the magnetic field are neglected. The design of the coils [9] is not yet completed.

The first category covers the dead zones due to the support structure of the iron plates (see figure 5.6).

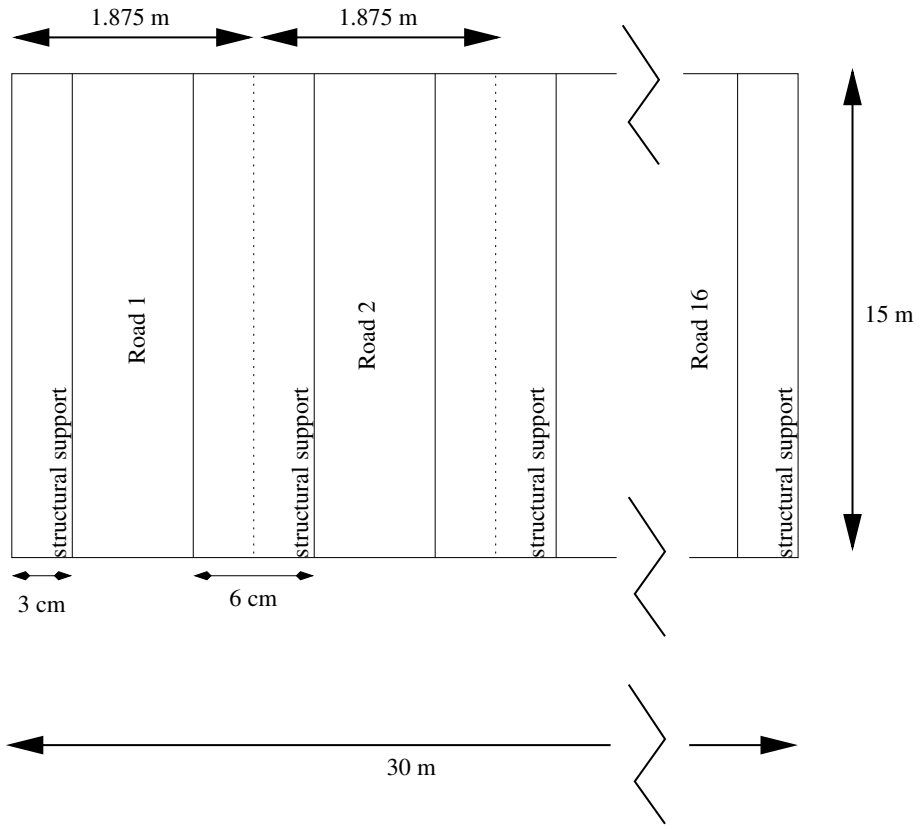

Figure 5.6: Top view of the support structure of an iron layer. The columns parallel to the **X** coordinate are 3 cm wide at the edges of a plane and 6 cm wide every 1.875 m.

The support structure consists of 6 cm thick columns every 1.875 m and 3 cm thick columns at the edges of the detector. This type of dead zone is parallel to the **X** direction and has only an effect on the **Y** hit information.

The second category marks hits situated in dead zones due to the GSC structure (see figure 3.5) and due to the combination of the GSCs to a readout plane (see figure 3.8). Due to the simulation of the hits without dead zones and in a continuous strip pattern, the impact of the dead zones can only be given approximately. In the following, the size and position of the coarse structure of iron layer support dead zones are taken as fixed parameters. Also the number of units and GSCs in the composition of a detector layer are defined according to the detector description (see 3.2.3). Therefore, the

individual size of a GSC has to be adopted. The approximated width of the GSC chambers is calculated by dividing the distance between the support structures (see figure 5.6) with the fixed number of chambers in a unit: 6. According to this chamber pattern, all dead zone positions are calculated.

The GSC glass plates are held apart by spacers. At the positions of the spacers, a passing particle can not induce a spark. Therefore, the spacers represent dead zones with effect on the **X** hit information. The spacers are 15 cm long and 2 mm thick. This results in a non-continuous dead zone. To avoid this complication, the length of the spacers is scaled to the width of the GSC (see figure 5.7). In the course of this approximation, also the thickness is altered to preserve the total area of a spacer.

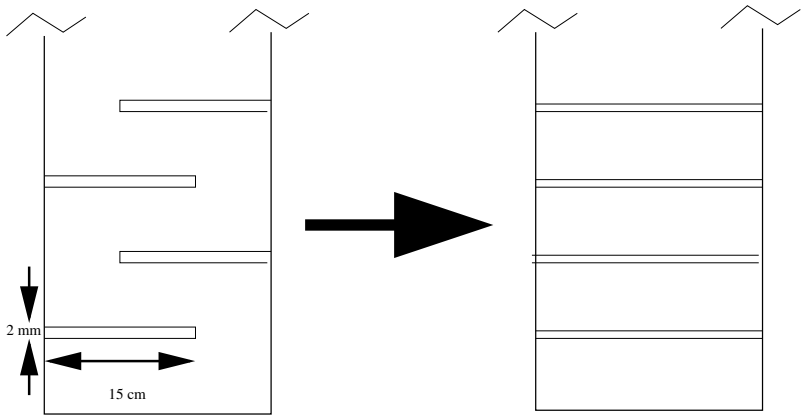

Figure 5.7: The spacers which hold the plates apart are 15 cm long and 2 mm wide. This non continuous dead zone is transformed to a continuous dead zone by stretching the spacer to the complete width of the chamber. The dead zone area is preserved by changing the spacer width accordingly.

The spacers are clamped to the glass plates at their edges (see figure 5.8) and represent a dead zone with effect on the **Y** hit information.

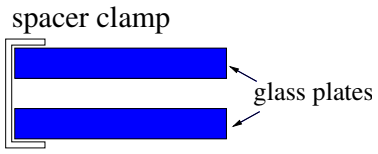

Figure 5.8: The dead zones induced by the spacer clamps at the edges of the glass plates have an effect on the **Y** hit information.

In addition, the thickness of the Noryl envelope is combined with the dead zones due to the spacer clamps to one dead zone of the thickness of 6 mm.

With effect on the **X** hit information, the dead zones due to the end-caps (see figure 3.6) are merged with the dead zone due to the connector gap between the units. The resulting dead zone has a width of 6 cm (see figure 5.9).

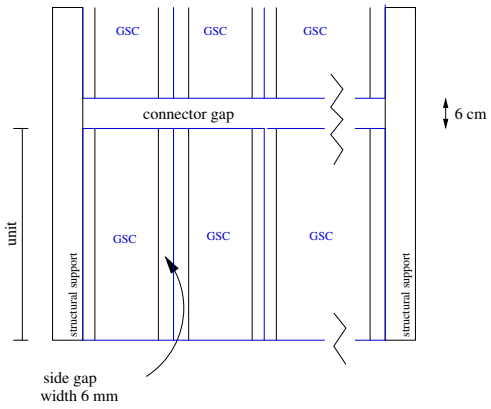

Figure 5.9: Sketch of the dead zones according to the end-caps of the GSC and the support gap between two units. The width of this dead zones is 6 cm in **X**. In addition, the dead zone according to the spacer clamps and the envelope width in **Y** are displayed.

Also the total efficiency of the chamber is taken into account. A flat distribution according to the chamber efficiency of 92% randomly excludes hits from the analysis. The efficiency is taken from the test setup results (see 4.5) and presents a conservative chosen value. The efficiency expected for the MONOLITH detector is higher [9].

A further complication of the described dead zone procedure is related to the positions and sizes of the dead zones. In relation to the strip width of 3 cm, the width of a dead zone or its position does usually not fit in the strip pattern (see figure 5.10). Considering for example the position of the left edge of a dead zone, the position is normally not situated at the border between two readout strips which would allow to distinguish exactly a strip in the dead zone from a valid strip. In the normal case, the edge of a dead zone is situated in between the 3 cm of a strip. But the available hit information from the event sources require a clear decision which strip is valid and which strip is situated in a dead zone. This requirement is implemented by a procedure using random numbers. The part of the 3 cm of the strip

covered by the dead zone edge is calculated. A flat distribution between 0 and 1 generates a reference. If the reference number is greater or equal to the calculated strip part of the edge, the strip which includes the left edge of the dead zone belongs to the dead zone. In the other case, the strip is a valid strip. This procedure is repeated for each calculation of position or size and a new reference is generated for each repetition.

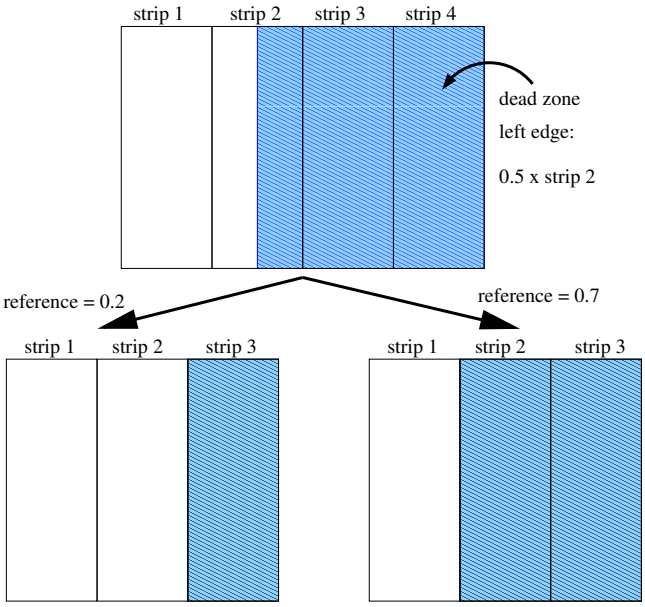

Figure 5.10: The position of the left edge of a dead zone is not situated between two strips. The strip which belongs to the dead zone can not be distinguished from the valid strip. A reference generated by a flat distribution between 0 and 1 decides whether strip 2 belongs to the dead zone or not.

The visualization of the dead zone procedure is again given by an event display which is further discussed in 5.5.5. In contrast to the visualization of the read procedure, the dead zone procedure is visualized by the realistic event display according to the event including the dead zones, the realistic event.

5.5.4 Trigger Procedure

To investigate the response of a trigger algorithm to an event out of an event sample, the hit pattern of the realistic event has to be transformed to the trigger pattern by combining the hits of a road per layer to one trigger channel (see figure 5.1). This is done by the trigger procedure. Also the application

of the trigger is performed by this procedure by dividing the hit pattern into units of consecutive layers per road (UNIT) with a certain overlap (OVERLAP) and giving a positive response if the required hit number condition in a unit (HIT) is fulfilled. The visualization is again discussed in 5.5.5.

5.5.5 Event Displays

The different steps of the data processing are visualized by corresponding event displays.

The visualization of the read procedure (see 5.5.1) is represented by the **event display** (see figure 5.11).

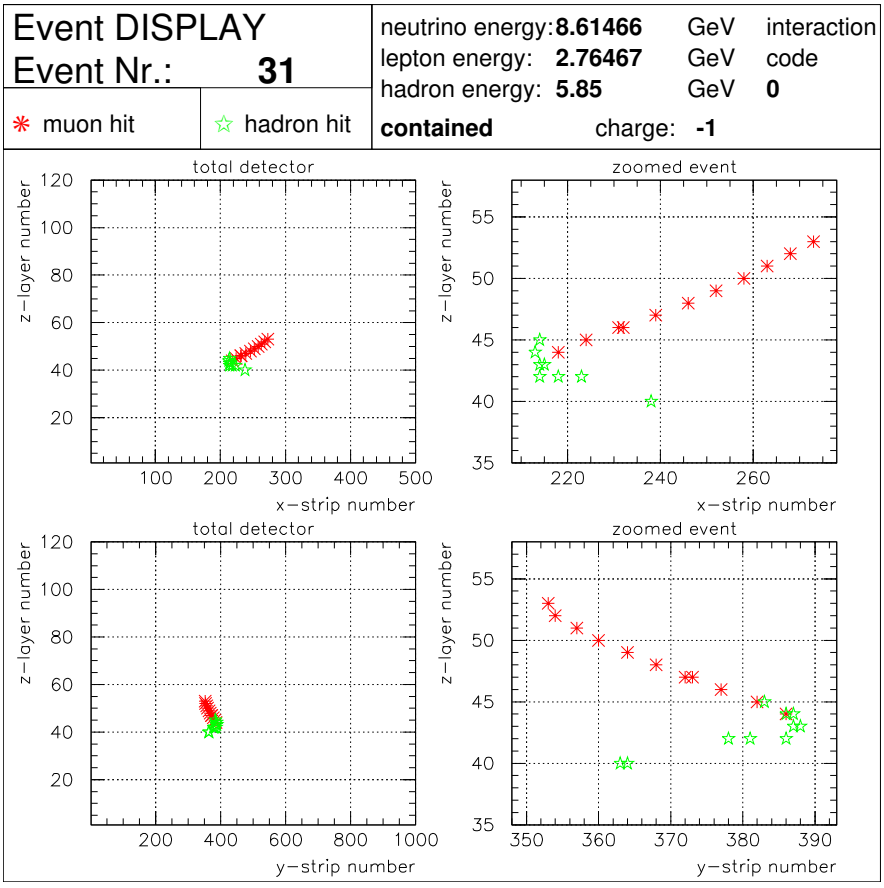

Figure 5.11: Example event display which presents all relevant informations of an event from an event sample (for detailed discussion see text).

The three dimensional hit pattern of an event is projected to the **X-Z** plane and the **Y-Z** plane. The event is displayed in the total detector

projections including all readout strips and in zoomed projections. The hits in the detector are separated into muon and hadron hits. Furthermore, the energy of the neutrino, the muon and the hadronic final state is given, as well as the interaction code of the neutrino interaction. The muon is characterized whether it is contained in the detector volume or outgoing and the charge of the muon is given.

Since the cut procedure only sets flags whether an event fulfills the required cuts or not (see 5.5.2), the effect of the dead zone procedure is visualized by the **realistic event display** (see figure 5.12).

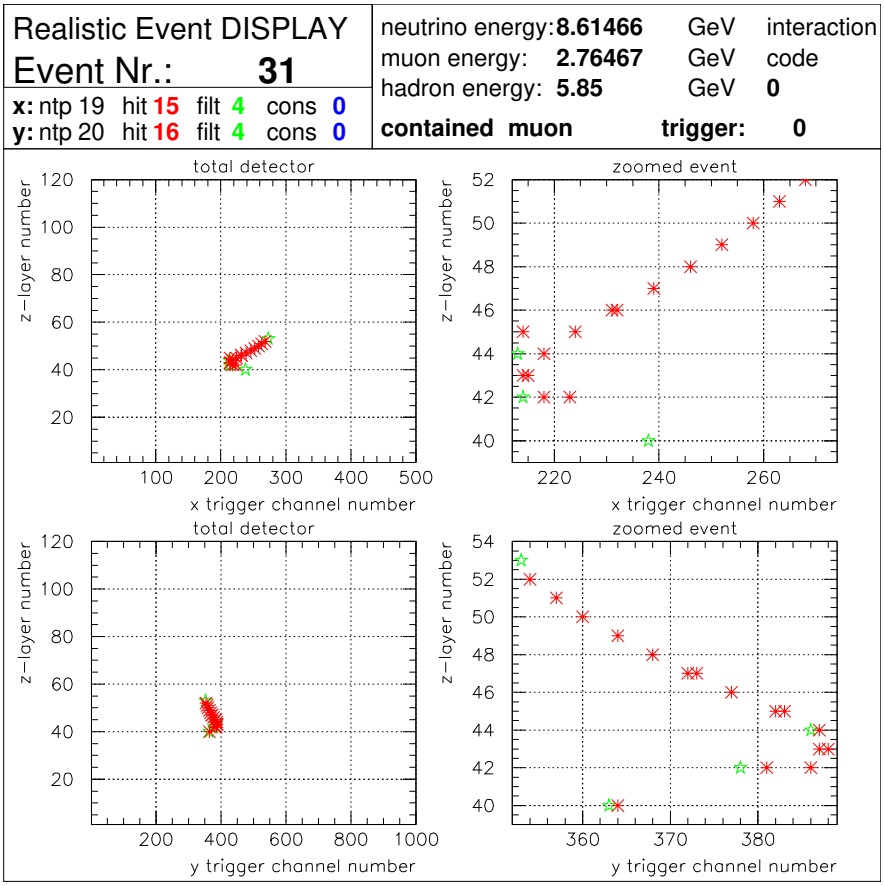

Figure 5.12: The realistic event display shows the impact of the dead zone procedure on the event in contrast to the event display (see figure 5.11) (for detailed discussion see text).

The two projections of the three dimensional hit pattern including the zoomed versions present hits distinguishing valid hits and hits situated in

dead zones. In addition, the numbers of the two hit categories are given for the two projections. Also the numbers of hits which do not fulfill the consistency requirements (see 5.5.3) are given. In addition, the trigger flag for an exemplary trigger parameter combination is given.

The visualization of the trigger procedure is given by the **trigger display**. According to the trigger design (see 5.3), only the **Y-Z** projection is displayed including the valid hits and hits situated in dead zones, which is the only difference to the realistic event display.

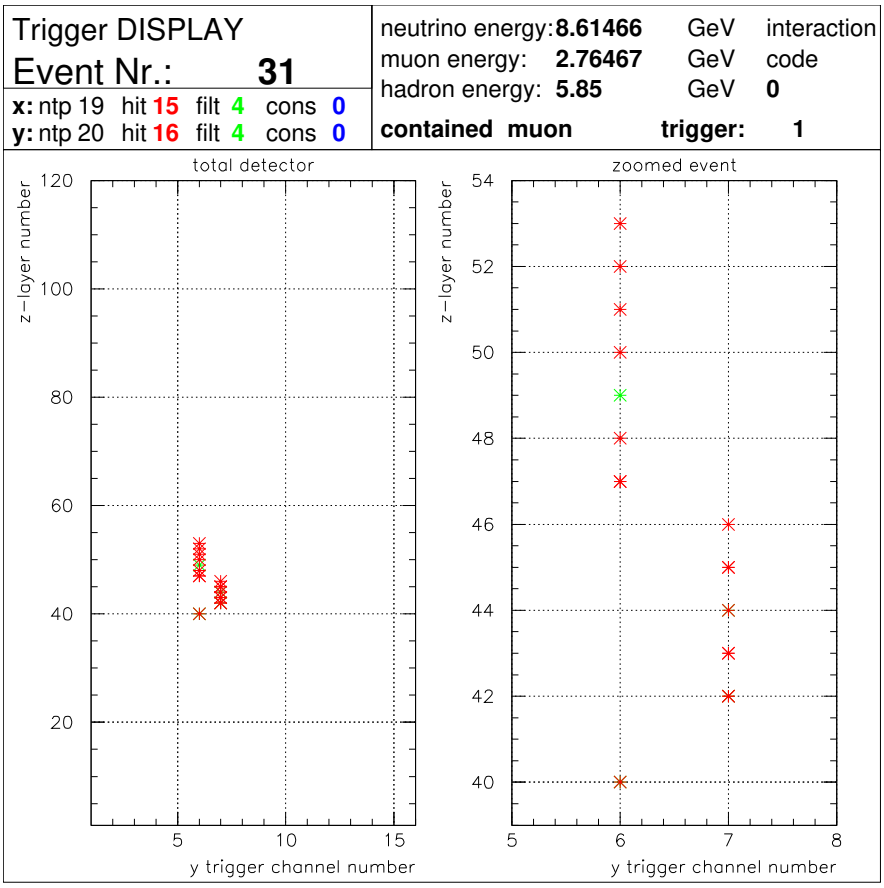

Figure 5.13: The trigger display shows in contrast to the realistic event display (see figure 5.12) only the trigger pattern in the **Y-Z** plane which is relevant for the trigger (see 5.3) (for detailed discussion see text).

5.6 Trigger Investigation

For the optimization of the trigger, the described data sources (see 5.4) and presented procedures (see 5.5) are used. In the beginning, several trigger parameter combinations are investigated (see 5.6.1) according to the requirements of the MONOLITH trigger. Resulting from the investigation, an optimized trigger parameter combination is determined which is referred to as the standard trigger algorithm. In addition, the performance of the standard trigger algorithm is discussed with respect to the variation of detector parameters (see 5.6.2). This allows the adaptation of the trigger parameter combination to future changes of the detector.

5.6.1 Trigger Optimization

The optimization of the trigger parameter combination consisting of the number of consecutive layers in a unit (UNIT), the required hits in a unit (HIT) and the overlap between adjacent units (OVERLAP) (see 5.3) is performed in the following. The different trigger parameter combinations are investigated with respect to their performance concerning rate and efficiency. The dependence of the efficiency on the combination is derived from the application of the different trigger parameter combinations to the events from the neutrino sample (see 5.4.1). The dependency of the trigger rate on the combination is investigated by the application of the different trigger algorithm to the events from the noise simulation (see 5.4.2).

In this investigation, only trigger parameter combinations with a unit size of 5 layers are investigated. A unit size of 6 layers is not realizable due to the constraint of the hardware (see 5.3). Parameter combinations of a unit size of 4 are also excluded from the analysis. In analogy to the statistical studies of the algorithm consisting of 2 required hits (HIT=2) in a 5 layer wide unit (UNIT=5) at an overlap of 4 (OVERLAP=4) (see 3.2.3), the parameter combination which requires 2 hits (HIT=2) in a 4 layer wide unit (UNIT=4) at an overlap of 3 (OVERLAP=3) would result in a trigger rate incompatible to the requirement of a trigger rate less than 1 kHz. The same combination with 3 required hits (HIT=3) is excluded due to the smaller efficiency with respect to the combinations investigated in the following.

To optimize the trigger parameter combination with respect to the remaining two parameters, the required hits in a unit (HIT) and the overlap between two adjacent units (OVERLAP), the optimization problem is divided up into two parts consisting of the optimization of only one parameter by taking the other parameter as constant. In the beginning, the number of required hits (HIT) is optimized at fixed overlap (OVERLAP=3) followed by

the optimization of the overlap at the optimized number of required hits. In the end, a more detailed investigation of the optimized trigger is presented.

Optimization of Number of Required Hits

Starting with the optimization of the number of required hits in a unit (HIT), the overlap of adjacent units is kept fixed at 3 (OVERLAP=3). In addition to the dependency of the trigger rate from the different trigger parameter combinations with the number of required hits in a unit of 1,2,3 and 4, the trigger rates of the cosmic background (see equation 5.2) and the expected trigger rate from neutrino interactions (see equation 5.1) are given (see figure 5.14).

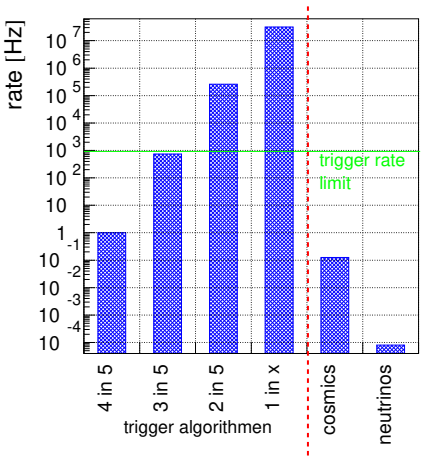

Figure 5.14: Dependence of the trigger rate on different parameter combinations with fixed overlap (OVERLAP=3). The cosmic background trigger rate and the expected neutrino trigger rate are displayed.

The trigger rate for the combination with 2 required hits in a unit (HIT=2) is about 257 kHz (see figure 5.14). This rate differs from the expectation of the investigation in 5.3 which expects a trigger rate of 377 kHz. The difference originates in the dead space treatment (see 5.5). After the noise event generation (see 5.4.2), the event sample consists only of events which fulfill the trigger algorithm requirement of 2 hits in a unit of 5 layers. Without the data processing chain, the application of the same trigger parameter combination should result in a comparable trigger rate. The deviation results from the dead zones procedure (see 5.5.3), which marks only about 82% of all hits valid. The resulting trigger rate after the marking process is reduced by a factor of about $(0.83)^2 \approx 0.7$, which

is compatible with the total reduction of the hits in the neutrino sample (377 kHz $\times$ 0.7 = 264 kHz).

The further performance of the compared algorithms is studied with the dependence of the efficiency on the trigger parameter combinations (see figure 5.15). The efficiency is derived by taking into account all neutrino events with fulfilled trigger condition divided by all events including an energy threshold of 2 GeV. Two studies were performed with different sub-samples of the neutrino sample, one including the cuts for the oscillation pattern analysis (see 5.5.2) and the requirement of only ν_μ-CC interactions (interaction code 0). The second only requires ν_μ-CC interactions.

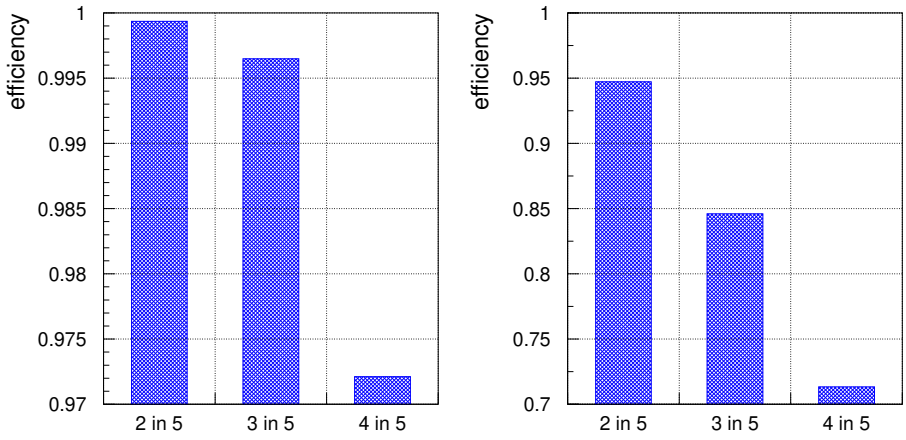

Figure 5.15: Dependence of the efficiency on different trigger parameter combinations with fixed overlap (OVERLAP=3) and an energy threshold of 2 GeV for ν_μ-CC interactions. *left:* efficiency dependence on combination including oscillation pattern analysis cuts, *right:* efficiency dependence on combination without any specific cuts.

Resulting from the two investigations, the optimized number of required hits in a unit is given by **3**. This combination results in the highest efficiency compared to the other combinations at a trigger rate compatible with the required maximal trigger rate of 1 kHz. For the following optimization of the overlap between adjacent units (OVERLAP), the optimized number of 3 required hits in a unit (HIT=3) is kept fixed.

Optimization of the Overlap of Adjacent Units

The investigation of the still not optimized trigger parameter , the overlap (OVERLAP), is performed by fixing the number of required hits in a unit with respect to the parameter combination optimized so far (UNIT=5, HIT=3). Apart from the efficiency influence, the overlap between adjacent units has a large impact on the electronics effort. The overlap defines the total number of units in a road and the more units are in a road the more electronics is needed for the trigger. In analogy to the described investigation, the dependence of the trigger rate on the number of layers overlap between adjacent units is analyzed (see figure 5.16).

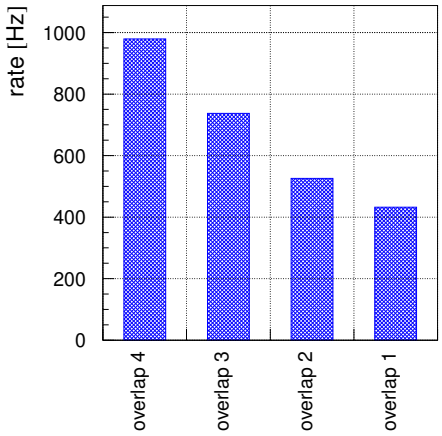

Figure 5.16: Dependence of the trigger rate on different numbers of layers overlap according to the so far optimized trigger parameter combination (UNIT=5, HIT=3).

The overlap optimization is continued by the investigation of the dependence of the efficiency on the overlap according to the trigger parameter combination optimized so far (see figure 5.17).

Indicated from the investigations, the trigger parameters combination with an overlap of 1 layer results in the lowest electronics effort but also in the lowest efficiency compared to the other investigated combinations whereas the combination with an overlap of 4 layers shows the highest efficiency and the highest electronics effort.

The optimized combination is given by an overlap of 2 layers (OVERLAP=2). The efficiency of this combination is comparable to the efficiencies of combinations of larger overlap but results in the smallest electronics effort compared to the combinations with higher overlap. The optimized overlap

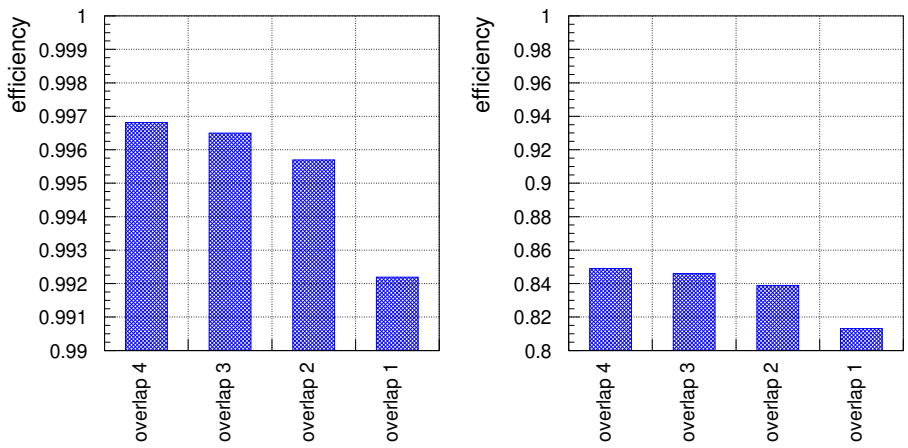

Figure 5.17: Dependence of the efficiency on the overlap according to the so far optimized trigger parameter combination and an energy threshold of 2 GeV for ν_μ-CC interactions. *left:* efficiency dependence on overlap including oscillation pattern analysis cuts, *right:* efficiency dependence on overlap.

reduces the trigger rate to 526 Hz compared to the trigger rate of the so far optimized trigger parameter combination of 773 Hz. The efficiency of the optimized trigger parameter combination (UNIT=5, HIT=3. OVERLAP=2) for a neutrino energy threshold of 2 GeV for ν_μ-CC interactions is about 99.6% including oscillation pattern analysis cuts and 84.0% without.

The optimized trigger algorithm is compatible with the stated requirements of minimal electronics effort at maximal efficiency and a trigger rate below 1 kHz and consist of:

- a unit formed of **5** consecutive layers within a single road,
- a required number of **3** hits in a unit,
- an overlap of **2** layers between adjacent units.

Efficiency Investigation

For further qualification of the optimized trigger algorithm, a detailed study of the efficiency is performed. The efficiency of the trigger algorithm is investigated dependent on the energy of all three possible constituents of a ν_μ-CC interaction. The results are given including the cuts for the oscillation pattern analysis and without specific cuts (see figure 5.18).

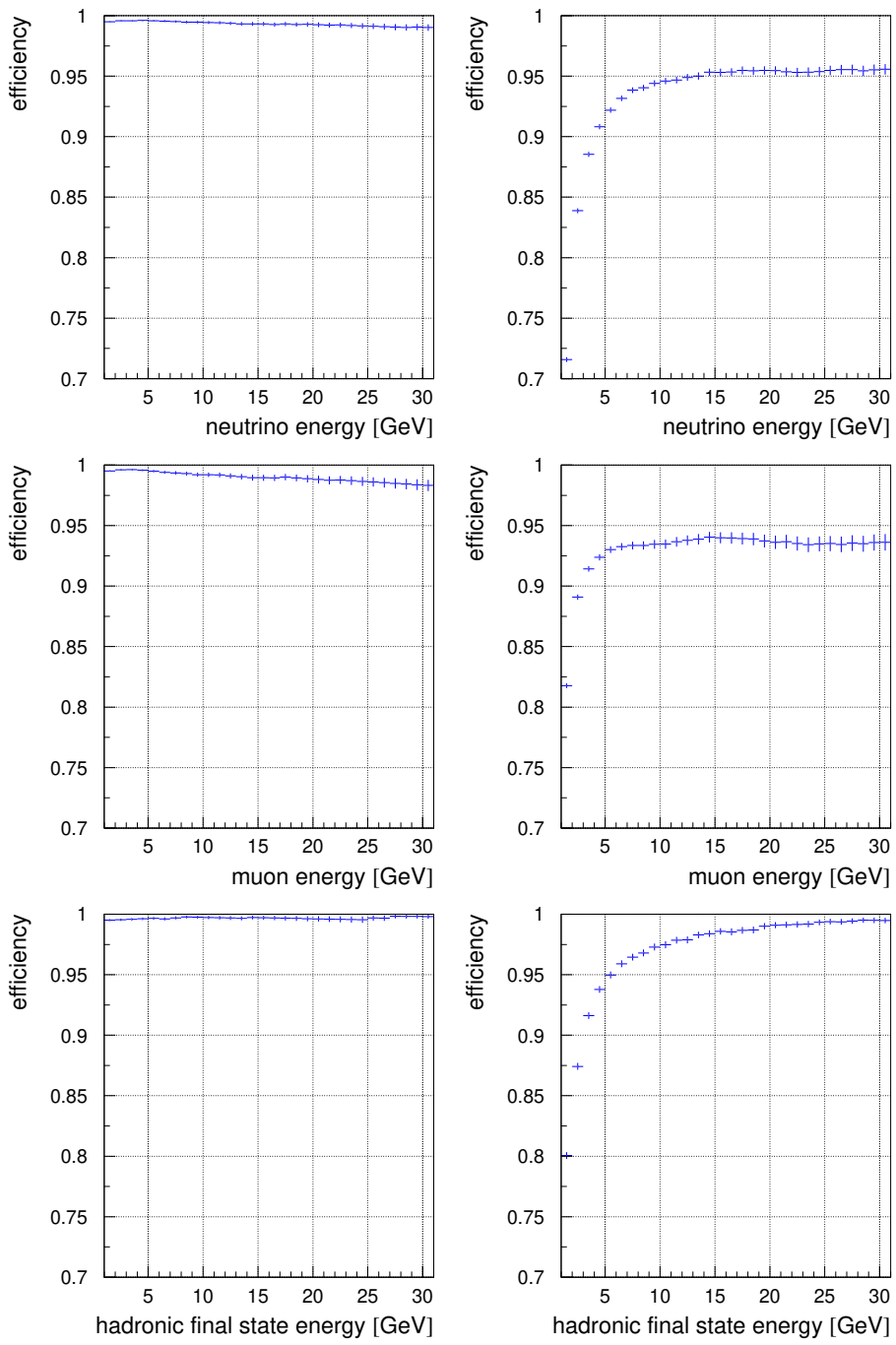

Figure 5.18: Efficiency for events with energy greater than an energy X depending on the energy X for ν_μ-CC interactions. *left:* efficiency dependence on energy including analysis cuts, *right:* efficiency dependence on energy. *top row:* neutrino energy dependence, *center row:* muon energy dependence, *bottom row:* hadronic final state energy dependence (all plots including binomial error bars)

The efficiency as a function of the energy without any specific cuts is very good. Especially for neutrino events with an energy above 4 GeV, the efficiency is more than 90%. The energy dependencies including oscillation pattern analysis cuts starts at an excellent efficiency of 99% and indicates a decrease of the efficiency for high energy events. This is mainly an effect of the trigger on high energy events with large angle θ (see 2.9).

5.6.2 Dependence on Detector Design

The resulting optimized trigger is derived from a specific detector parameter set, which is stated by the MONOLITH detector design (see 3.2.1) [9] and by results from the test setup (see 4). To adapt the results of the investigation of the optimized trigger to possibly changed detector parameters, the performance of the optimized trigger is investigated with respect to variations of the trigger time and of the single hit rate of the GSC.

The neutrino sample (see 5.4.1) depends only on parameters which can not be changed in the course of this investigation. Since efficiency investigations are performed in this thesis only by the application of the trigger on the neutrino sample, an explicit investigation of the dependence of the efficiency on detector parameters can not be realized.

The trigger rate dependence investigations are performed by using the generated noise event sample (see 5.4.2). The generation includes amongst other things two parameters, which can be varied, the trigger time and the single hit rate of the GSC. However, since the maximum distance a particle can travel within a trigger unit is about 15 m, it is expected that reducing the trigger time to 50 ns should not affect the efficiency.

In the following, an investigation of the dependence of the trigger rate on the trigger time and on the GSC single hit rate is presented, using the optimized trigger parameter combination.

Several noise event samples are generated with a fixed single hit rate of 580 Hz and trigger times from 10 ns to 100 ns.

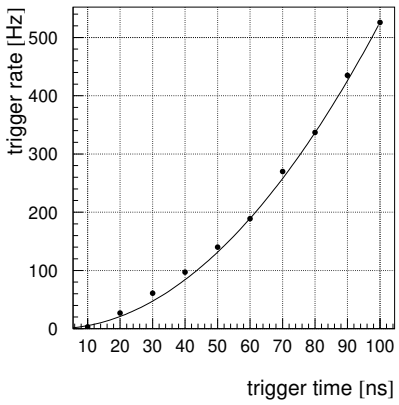

Figure 5.19: The variation of the trigger time using the optimized trigger parameter combination induces a change of the trigger rate which can be approximated with equation 5.9.

For instance, reducing the trigger time to 50 ns would reduce the rate to 140 Hz.

For the single hit rate dependence investigations, several noise event samples are generated with a fixed trigger time of 100 ns and single hit rates from $200\frac{\mathrm{Hz}}{\mathrm{m}^2}$ to $580\frac{\mathrm{Hz}}{\mathrm{m}^2}$.

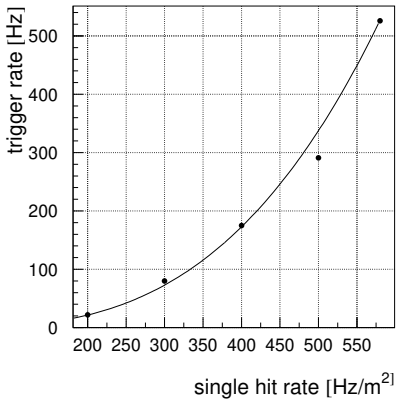

Figure 5.20: The approximation of the dependence of the trigger rate on the single hit rate can be approximated by equation 5.10.

A noise reduction of 20% would reduce the rate by about a factor 2.

The statistical approach of the standard trigger algorithm results in the following dependency of the trigger rate I_{trigger} on the single hit rate I_{single} and the trigger time t_{trigger}:

$$I_{\text{trigger}} \propto I_{\text{single}}^3 \times t_{\text{trigger}}^2 \tag{5.8}$$

The dependence of the trigger rate on the trigger time (see figure 5.19) using the standard trigger algorithm (UNIT=5, HIT=3, OVERLAP=2) can be approximated by:

$$I_{\text{trigger}} = 0.053 \cdot t_{\text{trigger}}^2 \tag{5.9}$$

with the trigger rate I_{trigger} and the trigger time t_{trigger}.

The trigger rate dependence on the single hit rate of the GSC (see figure 5.20) can be approximated by :

$$I_{\text{trigger}} = 2.7 \cdot 10^{-6} \cdot I_{\text{single}}^3 \tag{5.10}$$

with the trigger rate I_{trigger} and the single hit rate of a GSC I_{single}.

The presented investigation describes the dependence of the performance of the optimized trigger parameter combination on the possible variation of detector parameters. Indicated by these results, a possibility can be given how to reduce the trigger rate by changing the single hit rate of the GSC and the trigger time. The variation can only be realized if it does not influence the performance of the MONOLITH detector according to the goals of MONOLITH (see 3.1.1).

5.6.3 Result

The presented structural design of the MONOLITH trigger algorithm (see 5.3) is investigated using the described data sources (see 5.4) and the presented data processing procedures (see 5.5). The investigations of the trigger (see 5.6) show that the structural design of the trigger fulfills the requirements of the MONOLITH project on the trigger and the optimization of the trigger results in the optimized trigger parameter combination of 3 required hits in a unit of 5 consecutive layers within a single road with an overlap of 2 layers between adjacent units. The efficiency of the trigger for neutrino events with an energy threshold of 2 GeV is 99.6% including the neutrinos oscillation pattern analysis and 84.0% without any specific cuts and is compatible with the requirement of an efficiency near to 1. Also the electronics effort is reduced to a reasonable amount.

In the course of the presented investigations, the dependence of the trigger performance on the variation of several detector parameters (see 5.6.2) is investigated if the investigation of the variation can be realized in this thesis. The results give a guidance to the variation of the trigger performance at changed investigated detector parameters. For example, if the trigger time is reduced to 50 ns at a single hit rate of the chamber of 580 $\frac{\mathrm{Hz}}{\mathrm{m}^2}$, the trigger rate can be reduced to about 140 Hz.

Chapter 6

Summary and Conclusion

This thesis describes the development of the trigger algorithm for the MONOLITH experiment. A related long term test using a single GSC setup is presented.

The MONOLITH project is proposed to prove the hypothesis of atmospheric neutrino oscillations and to improve the measurements of Super-Kamiokande.In the course of this thesis, an introduction of the mechanism of neutrino oscillations is given. The MONOLITH project is presented in the context of atmospheric neutrino oscillations including a description of the used detector concept.

The practical part of this thesis consists of a long term test of a single active component of MONOLITH, the glass spark chamber (GSC). The test setup is described and a status report of the long term test is given. The noise rate and the efficiency of the GSC are determined and directly taken as input for the trigger development:

Noise rate: 580 $\frac{\mathrm{Hz}}{\mathrm{m}^2}$, consistent with expectations.

Efficiency of GSC: 92% (This value represents a lower limit of the efficiency of the chamber. The efficiency expected by the MONOLITH collaboration is higher.).

These numbers correspond to stabilized initial values and improved slightly during the long term test. The time resolution of 2 ns is confirmed. In general the test establishes the long term stability of this type of GSC, which had not been investigated so far.

For the development of the trigger algorithm, the structural design is described and the three main parameters of the algorithm are presented:

UNIT: Number of consecutive layers in a unit.

HIT: Number of required hits in a unit.

OVERLAP: Number of layers overlap between adjacent units.

For the investigation of several trigger parameter combinations, two event sources are used. A Monte Carlo neutrino event sample used for efficiency analyses is described. A noise simulation is generated to investigate the trigger rate. These sources are processed including an implementation of dead zones. Several event displays visualize the different steps of the data processing.

The optimization of the three algorithm parameters results in the standard trigger algorithm. The standard trigger algorithm consists of units of 5 consecutive layers constrained to a single road with an overlap of 2 layers between adjacent units and requires 3 hits in a unit:

1. UNIT=5
2. HIT=3
3. OVERLAP=2

A detailed investigation with a trigger time interval of 100 ns results in an efficiency of 99,6% for ν_μ-CC events which fulfill the cuts for the atmospheric neutrino oscillation analysis, and 84% for ν_μ-CC events with $E_\nu > 2$ GeV without any specific cuts. The trigger rate is dominated by random triggers caused by GSC noise. A resulting rate of 526 Hz is obtained.

The strong influence of the noise rate of the GSC and the trigger time on the trigger rate of the standard trigger algorithm is investigated. A reduction of the noise rate of about 20 % would result in the reduction of the trigger rate of about a factor of 2. On the other hand, a reduction of the trigger time to 50 ns decreases the trigger rate to 140 Hz. The described reduction of the trigger time is not expected to influence the efficiency of the standard trigger algorithm.

The investigated trigger algorithm fulfills the requirements of the MONOLITH trigger and is proposed to be realized.

Appendix A

Cosmics Trigger

The cosmics trigger (see 4.2) is used as a reference for the GSC signal. In the following, the cosmics trigger is shortly introduced and the calibration of the scintillators is described.

The trigger consists of two scintillators (see figure 4.1) which are denoted in the following as **N25** for the scintillator above the table and **N58** for the scintillator below the table.

The cosmics trigger provides a reference signal for a passing charged particle when both scintillators give a simultaneous signal.

The electronics setup (see figure A.1) consists of two linear fan-in-fan-out units for signal fan-out, two discriminators for background cut-off and generation of digital signals of the length of 50 ns and a logic unit for the coincidence signal as a logical 'and' of the two digital scintillator signals. The logic 'and' generates a digital signal if the two digital pulses of the discriminators overlap for at least 4 ns.

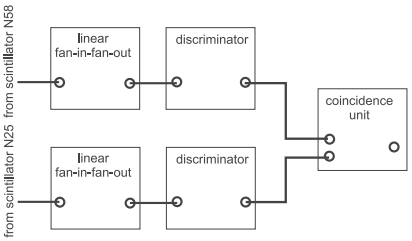

Figure A.1: Sketch of cosmics trigger electronics setup: the signal of the scintillators is passed through two linear fan-in-fan-out respectively for signal fan-out to the discriminators which perform a background cut-off and a generation of digital signals followed by a logic unit which delivers the coincidence signal.

To reduce the background noise rate of the scintillators, a calibration is performed to optimize the supply voltage and the discriminator thresholds for each scintillator. The scintillators are evaluated by their energy spectrum using a multi-channel-analyzer. A special electronics setup is needed to adapt the analog signals of the scintillators to the multi-channel-analyzer measurement (see figure A.2). The setup consists of a **signal chain** (see A.2) and a **gate chain** (see A.3).

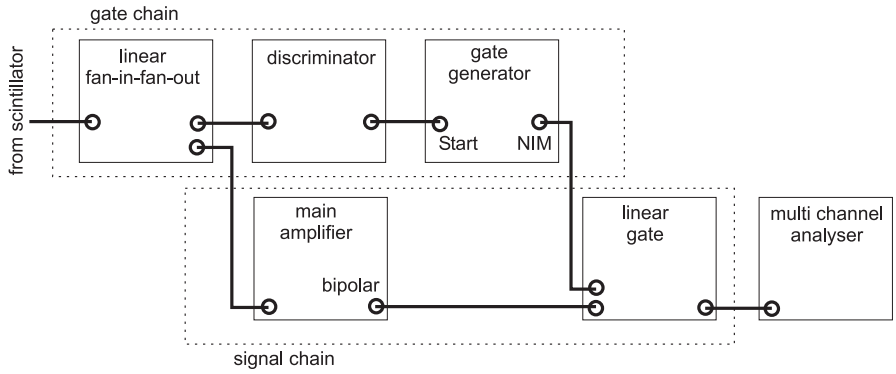

Figure A.2: Electronics setup to adapt the analog scintillator signals to the multi-channel-analyzer consisting of a **signal chain** (see A.2) for transformation of the energy content of a scintillator pulse (area of the pulse shape) to height of analog signal and a **gate chain** (see A.3) for the effect of the discriminator on the multi-channel-analyzer measurement.

A.1 Scintillator Signal

The scintillator signal consists of a pulse whose area depicts the deposited energy in the scintillator and indicates a passing particle (see figure A.3).

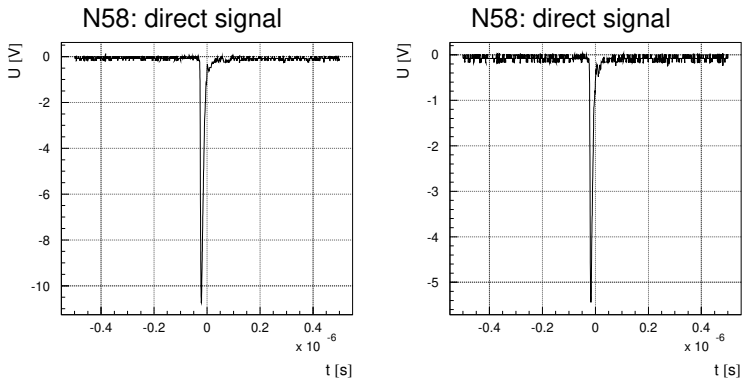

Figure A.3: Scintillator signal, area of pulse indicates deposited energy of passing particle

The following fan-in-fan-out distributes the scintillator signal (see figure A.4) to both chains. The signal height is not exactly duplicated but linearly scaled to the original signal height.

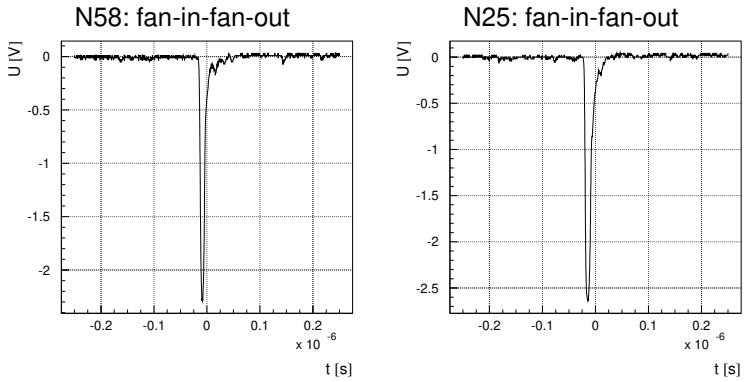

Figure A.4: Fan-in-fan-out signal, linear scaled scintillator signal.

A.2 Signal Chain

The energy content of the analog output of the scintillator pulses is depicted by the area of the pulse. This area is transformed to the amplitude of an analog signal with a main amplifier. In this case, the bipolar output of the amplifier is used (see figure A.5).

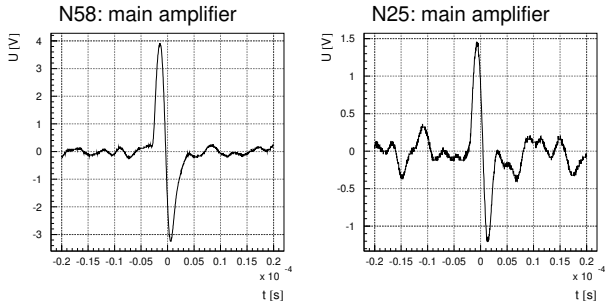

Figure A.5: Main amplifier signal, transformation of area of pulse (energy content) to signal amplitude height.

A.3 Gate Chain

To take the impact of the discriminator into account, the gate chain triggers the linear gate when a fan-in-fan-out signal of a height larger than the adjusted threshold reaches the discriminator.

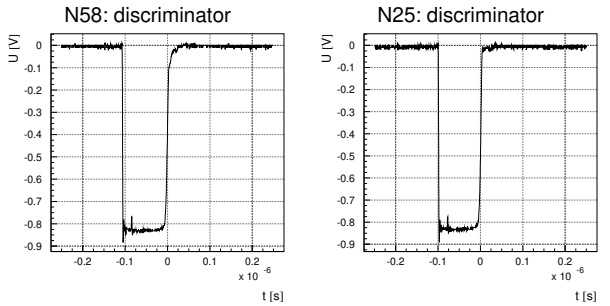

Figure A.6: Discriminator signal (digital NIM signal), occurs when scintillator signal height larger than threshold.

The signal of the discriminator (see figure A.6) is stretched by means

of a gate generator to open the gate for a sufficiently long time period for measuring the complete amplifier signal.

A.4 Calibration

The calibration of the scintillators cuts off the background noise. The normal expected spectrum of a scintillator measuring the signal of minimum ionizing particles consists of a Landau peak. Due to the low energy background noise, this Landau peak is not clearly visible in a measurement without a discriminator.

In the **first calibration step**, the high voltage supply of the scintillators is adjusted (see table A.4) so that apart from the noise peak a Landau shape at higher energies is visible (see figure A.7).

scintillator-number	**operation-voltage**
N25	$1,6\ kV$
N58	$1,8\ kV$

Table A.1: **First calibration step**: adjusted high voltage

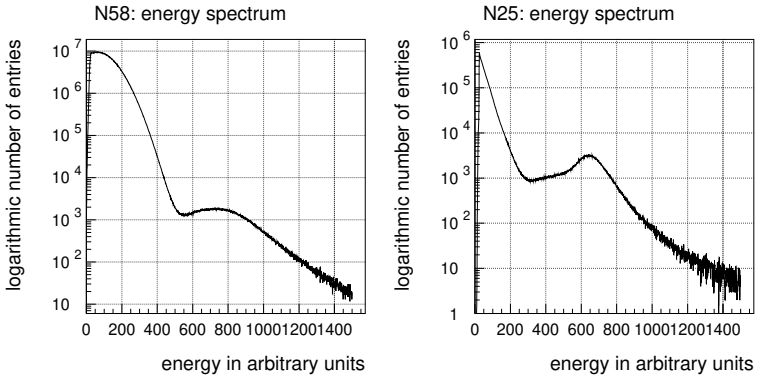

Figure A.7: **First calibration step**: adjusted high voltage supply of scintillators presents Laundau peak at higher energies superimposed to low energy background noise.

In the **second calibration step**, the discriminator threshold is adjusted (see figure A.8). Signals of an energy smaller than the minimum between the background noise peak and the Landau peak (see figure A.7) are cut off. The

remaining signals of these energies refer to the differences in the treatment of the signals. The discriminator considers the height of the amplitude of the signals, whereas the multi-channel-analyzer measures the energy of the signals and therefore the integrated area of the pulse. As a consequence, signals with a high amplitude and a small area open the gate. The energy content of the pulse is depicted by the area under the pulse shape. Therefore, these signals are displayed by the spectrum at low energies even though the background is correctly reduced by the discriminator.

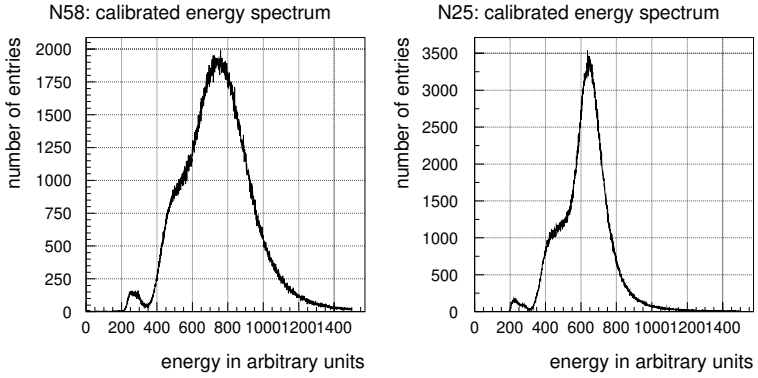

Figure A.8: **Second calibration step**: adjusted discriminator threshold between background and Landau peak for noise cut-off.

Appendix B

Fluxmeter Calibration

For calibration of the fluxmeter scale, the flux of Argon, which has comparable properties to the gas mixture, is controlled by the fluxmeter and measured by a soap bubble fluxmeter. A soap bubble of a defined diameter d driven by the adjusted flux climbs a defined distance s in a certain time t. The time t is measured by two light barriers. From this information, the gas flux is derived (see equation B.1).

$$\Phi = \frac{s\ \pi\frac{d^2}{4}}{t} \tag{B.1}$$

The calibration is performed with two different soap bubble fluxmeters which differ in their volume between the two light barriers (small soap bubble fluxmeter: $V = 1\ ml$, big $V = 20\ ml$) to cover a greater flux range (see figure B.1).

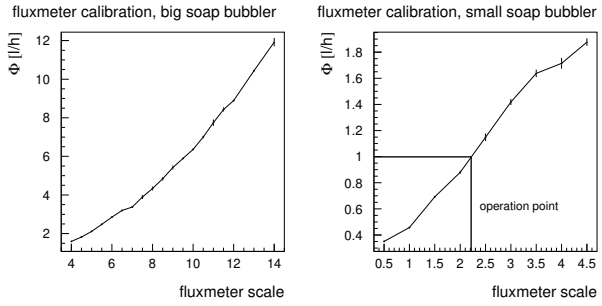

Figure B.1: Calibration of fluxmeter: *left:* with big soap bubble fluxmeter ($V = 20\ m$), *right:* with small soap bubble fluxmeter ($V = 1\ ml$). The chamber working point at a flux of $1\frac{l}{h}$ is indicated.

Bibliography

[1] H. Spiesberger, M. Spira and P. M. Zerwas, *The standard model: Physical basis and scattering experiments*, hep-ph/0011255;
D. Griffiths, *Introduction to elementary particles*, John Wiley & Sons, Inc., New York, 1987;
Schmüser, *Feynman-Graphen und Eichtheorien für Experimentalphysiker*, Springer, Berlin, 1995;
N. Schmitz, [4], p. 54 and references therein.

[2] J.N. Bahcall, P.I. Krastev, and A.Yu. Smirnov, Phys. Rev. **D 59** (1999) 046002;
N. Hata and P. Langacker, Phys. Rev. **D 56** (1997) 6107;
V. Castellani et al., Phys. Rep. **281** (1997) 309.

[3] G.L. Fogli et al., Phys. Rev. **D 55** (1997) 4385; Phys. Rev. **D 57** (1998) 5893.

[4] N. Schmitz, *Neutrinophysik*, Teubner, Stuttgart 1997.

[5] N. Schmitz, [4], p. 329 and references therein.

[6] N. Schmitz, [4], p. 322 and references therein.

[7] N. Schmitz, [4], p. 84 and references therein.

[8] Super-Kamiokande Collaboration, Y. Fukuda et al., Phys. Rev. Lett. **81** (1998) 1562;
Super-Kamiokande Collaboration, Y. Fukuda et al., Phys. Lett. **B 436** (1998) 33;
Super-Kamiokande Collaboration, Y. Fukuda et al., Phys. Lett. **B 433** (1998) 9.

[9] MONOLITH Collaboration, N.Y. Agafonova et al., *Proposal MONOLITH*, LNGS P26/2000, CERN/SPSC 2000-31, SPSC/M657, August 15, 2000.

[10] D. Karlen, *The number of light neutrino types from collider experiments*, Review of Particle Physics, D. E. Groom et al., Eur. Phys. J. **C15** (2000) 357.

[11] N. Schmitz, [4], p. 243 and references therein.

[12] L. Wolfenstein, *CP violation*, Review of Particle Physics, D. E. Groom et al., Eur. Phys. J. **C15** (2000) 115-116.

[13] N. Schmitz, [4], p. 252 and references therein.

[14] F. J. Gilman, K. Kleinknecht, B. Renk, *The Cabibbo-Kobayashi-Maskawa quark-mixing matrix*, Review of Particle Physics, D. E. Groom et al., Eur. Phys. J. **C15** (2000) 110-114.

[15] N. Schmitz, [4], p. 278 and references therein.

[16] N. Schmitz, [4], p. 284 and references therein.

[17] A. Geiser, *Neutrino physics with accelerators and beyond*, Rept. Prog. Phys. **63** (2000) 1779.

[18] Super-Kamiokande Collaboration, Y. Fukuda et al., official picture from http://www-sk.icrr.u-tokyo.ac.jp/doc/sk/photo/index.html

[19] KEK proposal E-362, K2K (KEK to Kamioka) neutrino oscillation experiment at KEK-PS, hep-ex/9803014.

[20] Y. Oyama (E362 (K2K) Collaboration), Proceedings of XXXV Rencontres de Moriond "Electroweak interactions and unified theories", Les Arcs, Savoie, France, March 11-18, 2000, hep-ex/0004015, and references therein.

[21] The NUMI-MINOS Project, NUMI-L-375 report (may 98); The MINOS Detectors TDR, NUMI-L-337 report (october 98 version).

[22] CDHS Collaboration, F. Dydak et al.,Phys. Lett. **B 134** (1984) 281.

[23] H. Sobel (Super-Kamiokande Collaboration), Proceedings of XIX International Conference on Neutrino Physics and Astrophysics (Neutrino 2000), Sudbury, Canada, June 16-21, 2000.

[24] Kamiokande Collaboration, Y. Fukuda et al., Phys. Lett. **B 335** (1994) 237.

[25] V. Barger et al., Phys. Lett. **B462** (1999) 109-114;
V. Barger et al., Phys. Rev. Lett. **82** (1999) 2640.

[26] R. Barbieri et al., P. Creminelli, and A. Strumia, Nucl. Phys. **B585** (2000) 28-44.

[27] E. Lisi, A. Marrone, and D. Montanino, Phys. Rev. Lett. **85** (2000) 1166-1169.

[28] G. Bencivenni et al., Nucl. Instr. and Method **A 300** (1991) 572.

[29] G. Bencivenni et al., Nucl. Instr. and Method **A 315** (1992) 507.

[30] M. De Deo et al., LNGS -95/39, June 1995.

[31] G. Bencivenni et al., Nucl. Instr. and Method **A 345** (1994) 456.

[32] G. Bencivenni et al., Nucl. Instr. and Method **A 332** (1993) 368.

[33] C. Gustavino et al., INFN/TC-99/14.

[34] K. Abe et al.,"Glass RPC Module for Belle Endcap KL/mu Detector", Proc. of IV Int.Workshop on Resistive Plate Chamber and Related Detectors, Napoli, Oct 15-16 1997; Ed. Sergio Ratti, Riccardo de Asmundis; A. Abashian et al.,Nucl. Instr. and Meth. **A 449** (2000) 112-124.

[35] M. De Deo, M. D'Incecco, C. Gustavino, G. Bencivenni and G. Felici, *Performance and simulation of glass spark counter*, INFN-TC-96-03, contributed to 3rd International Workshop on Resistive Plate Chambers and Related Detectors (RPC 95), Pavia, Italy, 11-12 Oct. 1995.

[36] M.D'Incecco et al:"Description of the Charge and Time card for Glass RPC detectors", MONOLITH note 004/00, unpublished.

[37] D.E. Groom et al., Eur. Phys. J. **C15** (2000) 151.

[38] I. Bloch, *Construction of the Cosmic Trigger for the MicroVertex Detector System Test*, lab report, Hamburg University, April 2001.

[39] The MACRO Collaboration, Phys. Lett. **B249** (1990) 149.

[40] The LVD Collaboration, Phys. Rev. **D58** (1998) 092005

[41] V. Agrawal, T.K. Gaisser, P. Lipari and T. Stanev, Phys. Rev. **D 53** (1996) 1314.

[42] T.K. Gaisser and T. Stanev, Phys. Rev. **D57** (1998) 1977-1982.

[43] M. Glück, E. Reya and A. Vogt, Z. Phys. **C 67** (1995) 433.

[44] P. Lipari, M. Lusignoli and F. Sartogo, Phys. Rev. Lett. **74** (1995) 4384.

[45] GEANT Detector Description and Simulation Tools, CERN Program Library, Long Writeup W5013.

Acknowledgments

In the beginning, I want to thank Prof. Dr. Robert Klanner for giving me the opportunity to do my diploma thesis in the interesting and challenging field of neutrino physics. I also want to thank him for his advice and for guiding me during the last twelve months.

I want to thank Prof. Dr. Beate Naroska for revising this diploma thesis as second corrector.

First of all, I want to thank Dr. Achim Geiser who supervised me during my diploma thesis. Dr. Geiser guided me through the work and helped me with his advice and his energetic assistance.

Special thanks to Carlo Gustavino who provided the glass spark chamber for the test setup and who contributed with Marco D'Incecco and Max de Deo to the setup of the single GSC. In addition, I want to thank Marco D'Incecco for his patience of answering all my questions.

I want to thank Tommaso Tabarelli and Francesco Terranova for providing the Monte Carlo event sample and for responding to my questions and all the other members of the MONOLITH collaboration for setting the framework for this thesis.

Special thanks also to Dr. Bernd Koppitz who provided me with his huge pool of hardware and who helped me with the cosmics trigger.

Furthermore, I want to thank Prof. Dr. Dr. h.c. Gunnar Lindström, Uwe Pein, Peter Buhmann, Petra Hendrikmann Verstegen and all the not mentioned members of the 'Nukleare Messtechnik' group of the 'II. Institut für Experimentalphysik der Universität Hamburg' for providing me help and support. In particular, I want to thank Dominik Dannheim, Ingo Bloch, Alberto Garfagnini, Jan Martens and Tancredi Carli who were always interested in what I was doing and helped me with their advice.

In the end, I want to thank everybody else who helped me during my diploma thesis.

Above all, I want to thank my family, my parents and my brother Dominic, who supported me, who kept me grounded in hard and in good times and who always gave me the feeling that I am doing the right thing.